Technische Universität München
Fakultät für Physik

Bachelor thesis in physics

3D Correlation Analysis for Like Sign pions $\pi^\pm\pi^\pm$ in $\pi+W$ Reactions at 1.7 GeV/c with HADES

3D-Korrelationsanalyse für identische $\pi^\pm\pi^\pm$ in $\pi+W$-Reaktionen bei 1.7 GeV/c mit HADES

Barbara Schweißhelm

Wednesday 16th September, 2015

Contents

Contents

Chapter 1

Introduction

In 1935, Yukawa predicted a particle, which should be the carrier of the strong force inside atomic nuclei. The idea of the pion was born. After twelve years, Perkins and Powell and Occhialini found experimental evidence of the pion almost at the same time [1] [2]. Now, 68 years later, the pion is still of scientific interest. A lot of resonances decay into a baryon and a pion or a baryon and a pair of pions. Studying the final state particles, one often cannot distinguish between primary pions and the ones originating from a short lived resonance. To investigate particles stemming from a baryonic resonance the inverse process can be used. This means to induce a reaction between a pion and a nucleon. The resonance is formed and its decay products can be measured, e.g. $\pi^- + p \rightarrow N^* \rightarrow n + \pi^- + \pi^+$. Due to the short lifetime of the pion ($\tau = 2,6 \cdot 10^{-8}$ s [3]) it is not possible to build a pion target. To study reactions between pions and other matter, e.g. nuclei, a pion beam is produced.

Pion beams have different properties than for example proton or photon beams. Photons produce new particles in the whole volume of a nucleus, because their interaction probability with nucleons is rather small ($\sigma \sim A$). The cross section for proton beams is smaller ($\sigma \sim A^{0.8}$), because many protons are absorbed at the surface of the nucleus producing secondary particles like pions, which penetrate the inner part of the nucleus. Pions on the other hand are assumed to be absorbed right at the surface of the nucleus ($\sigma \sim A^{2/3}$). All the reactions are illustrated in Figure 1.1 [4]. Although all these cross sections are model dependent, experimental results of the FOPI collaboration support that pions are absorbed right at the surface of a nucleus. In 2009, researchers of the FOPI collaboration analyzed experimental data of collisions of pions with different elements (C, Al, Cu, Sn and Pb) [5]. This data revealed the production of strange matter (kaons) in such reactions like $\pi^- + p$ or $\pi^- + n$ with the nucleons of the nucleus. The inclusive production cross section of K^0 appeared to depend on the mass number A of the corresponding target element, as it can be seen in Figure 1.2. They fitted this dependence with a power law function

$$\sigma(\pi^- + A \rightarrow K^0 + X) = \sigma_{eff} \cdot A^b. \tag{1.1}$$

The fit shows that the dependence of the production cross section of the mass number is approximately $A^{2/3}$ [5].
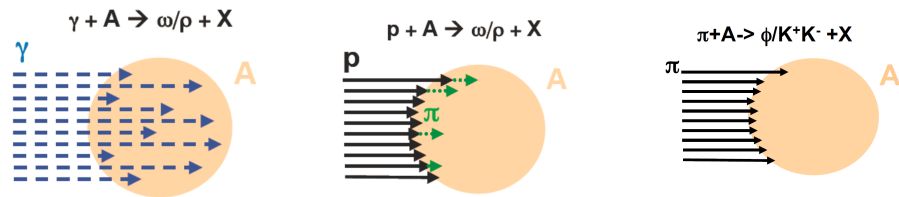
(a) A photon beam, which hits a nucleus has a low interaction probability with the nucleons. Production of new particles takes place in nearly the whole volume.

(b) A proton beam interacts strongly with the nucleus and the production of new particles takes place near the surface. It might also induce secondary pions.

(c) A pion beam, which hits a nucleus it interacts on the surface of the nucleus.

Figure 1.1: Differences in the reactions of induced by a photon, proton or pion beam with a nucleus are illustrated. [4]

In general, one can estimate the radius of a nucleus by $R \sim R_0 \cdot A^{1/3}$, where $R_0 = 1.3$ fm is approximately the size of one nucleon. This means that the surface of a nucleus, if it is assumed to be spherical, is proportional to $A^{2/3}$, since it scales with R^2. With the measurement of the FOPI collaboration it seems to be a valid assumption that pions are mostly absorbed at the surface of a nucleus.
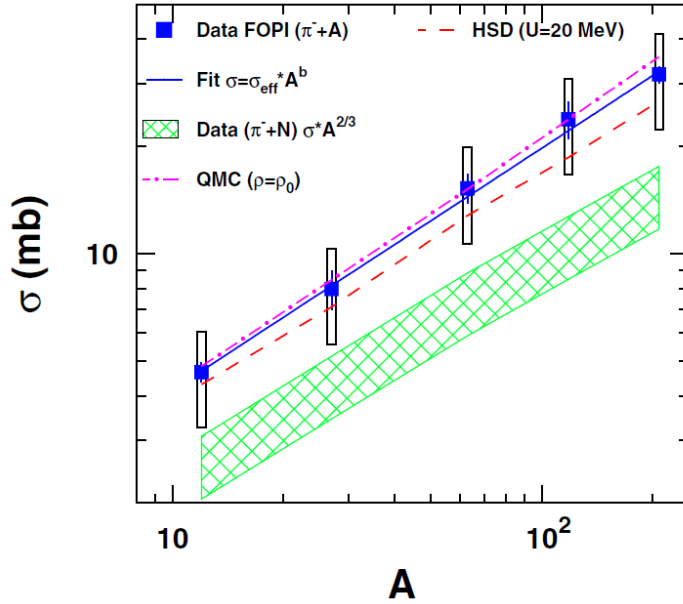
Figure 1.2: The mass number dependence of the inclusive production cross section of K_0. The data points, given by the blue squares, were measured by FOPI. The fit ($\sigma = \sigma_{\mathrm{eff}} \cdot A^b$) is represented by the solid line. The two dashed lines give two different model predictions, whereas the hatched area corresponds to the sum of the cross sections of the elementary processes scaled by the transverse size of the target nuclei [5].

Motivation of this work

Although the FOPI experiment suggests that the pions are absorbed right at the surface of the nucleus, we want to take a closer look at this assumption. If the pions are really absorbed at the surface, secondary pions would originate out of a source, which has the shape of a half, spherical shell like the side of the surface of the nucleus which faces the beam. With the help of a correlation analysis of these secondary pions it is possible to gain spatio-temporal information about the volume where their last interaction takes place before they fly into the detector. We can link the result of the correlation analysis to the volume of the absorption region of the primary pion, because we assume that the produced pions freeze out very close to their emission point. If this volume equals a half, spherical shell, one can conclude that the primary pions are absorbed at the surface of the nucleus.

The aim of this thesis is to gain further information about the absorption of pions at a tungsten nucleus by investigating the correlation of identical pion pairs in in a specific

reference frame, which allows to perform a three-dimensional correlation analysis. The used data was recorded with the High Acceptance Di-Electron Spectrometer (HADES) in July 2014. In the next section the experimental setup of the HADES experiment is described.

Chapter 2

HADES Experiment

The **H**igh **A**cceptance **D**i-**E**lectron **S**pectrometer (HADES) is located at the GSI Helmholtzzentrum für Schwerionenforschung in Darmstadt. With this fixed target experiment mostly dielectron production in pion, proton or heavy-ion induced collisions are studied. It was designed to investigate decays of the light vector mesons ρ, ω and ϕ. The lifetimes of these particles are in the same order of magnitude as the time of the compression phase in relativistic heavy-ion collisions. HADES is located at the SIS18 synchrotron which provides beam energies between 1-2AGeV for heavy-ions and up to 3.5 GeV for protons. Although HADES was constructed to investigate dilepton decays, it also allows the investigation of hadrons [6].

In the next section the important parts of the detector used for this analysis are briefly explained.
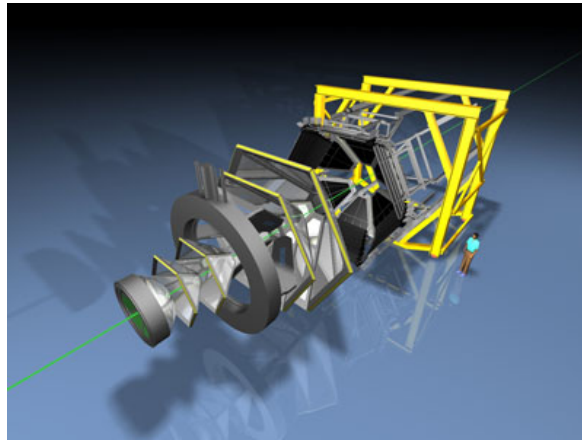
Figure 2.1: Expanded illustration of the whole HADES experiment. The beam axis is depicted as green line. The hexagonal structure is clearly visible [7].

2.1 Experimental Setup

Figure 2.1 shows an exploded view of HADES. The beam hits the target right in front of the RICH at the left end of the whole aperture. As it can be seen in the picture the whole experiment has a hexagonal structure, which means there are six identical sectors, arranged behind the target and around the beam axis. The azimuthal acceptance of HADES covers about 85% and its polar angle is covered by an interval from 15° to 85° [6]. A cross section of the aperture is given in Figure 2.2. Details about the analysed run, the target and the beam momentum are given in Table 4.1.
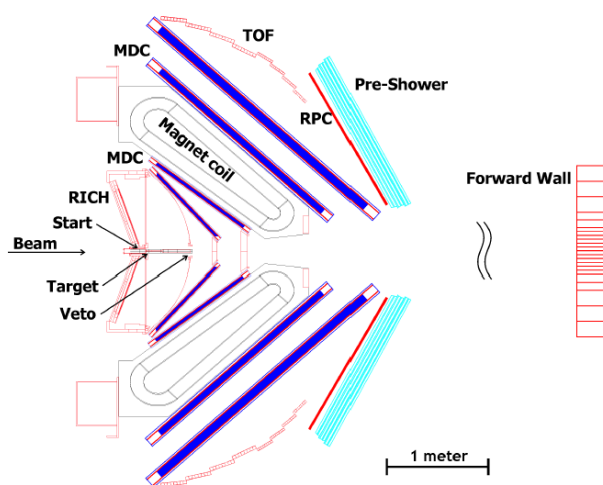
Figure 2.2: cross section of the HADES detector. [8].

2.1.1 Magnet

The magnet of the HADES experiment consists of six superconducting coils, which generate a toroidal magnetic field. The field strength is below B = 0.9 T to keep the experiment compact. Due to the Lorentz force the magnet forces charged particles to follow a circular path, which depends on their momentum and polarity. The curvature of the particle track can be used to calculate the momentum and the direction of it to determine the polarity of the particle. Therefore the magnet is an important part of the tracking system [6].
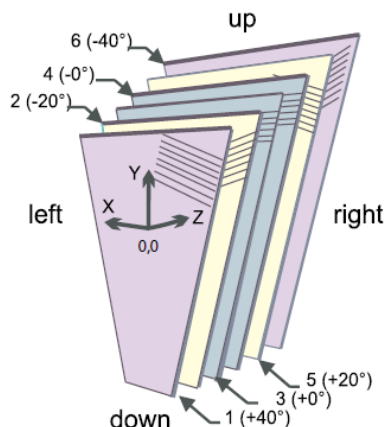
Figure 2.3: The six wire planes of the Multi-wire drift chambers of the HADES experiment are positioned in different angles to guarantee the best reconstruction. Every wire is rotated 20° [6].

2.1.2 Multi-wire Drift Chambers

The **M**ulti-wire **D**rift **C**hambers (MDC) are the most important part of the tracking system of the HADES experiment. They are arranged in the same hexagonal structure as the segments of the magnet. To gain information about the change of the momentum direction, charged particles receive from the magnet, there are two MDC planes (I, II) in front of and two (III, IV) behind the magnet. Each of these planes consists of four Mini-Drift Chambers. Each of these Mini-Drift Chambers consists of six wire layers, to guarantee a good track reconstruction also for high multiplicities. The six layers are arranged in different angles ($\pm 0°, \pm 20°, \pm 40°$), as it can be seen in Figure 2.3. With this structure the best spatial resolution in polar direction, the direction of the momentum direction change, can be achieved. Besides the momentum determination, the MDCs provide information over the energy loss of the traversing particle. Each charged particle looses energy by inelastic scattering with electrons bound in atoms of the detector gas. This energy loss is related to the time over threshold (ToT), which means the time an electronic signal exceeds a certain threshold. [6].

2.1.3 Time of Flight Detectors of the META System

The **T**ime **o**f **F**light detector (TOF), the **R**esistive **P**late **C**hambers (RPC) and the Pre-Shower represent the time of flight unity of HADES. They are an important tool to determine the hadron multiplicity and distinguish between hadrons and electrons [7].

- **Pre-Shower**: Electrons or positrons produce an electromagnetic shower in this part of the detector. Like it was already mentioned before, we are only interested in pions, so the Pre-Shower will be irrelevant for the following analysis.

- **TOF**: The TOF detector covers a polar acceptance of $44° < \Theta < 88°$. Its azimuthal geometry follows the same hexagonal structure like the magnet and the MDC. Since TOF is a scintillator, a traversing particle induces the emission of photons. The arrival time of these photons and the signal height, which they induce in the photomultipliers are measured. The signal height can be used to get an energy loss value, which can be used for particle identification (PID).

- **RPC**: The RPC detector replaced the TOFINO detector in 2009 and has very good time resolution with $\sigma_{\mathrm{RPC}} = 100$ ps. It covers an azimuthal angle range of almost 2π with oles due to the hexagonal structure and has a polar acceptance of $18° < \Theta < 45°$ [7].

2.2 Pion Beam

The usage of a pion beam allows the investigation of pion induced reaction. Because the pion beam is a secondary beam, additional components have to be introduced to the experimental setup. In the case of HADES it is produced with the help of a 10 cm thick beryllium-target and a primary beam of ^{12}C or ^{14}N from the Schwer-Ionen-Synchroton (SIS). Within this collision many particles are produced, but with a certain magnetic configuration of the beam optics it is possible to select the negative charged pions (π^-). These negative pion beam can then be used for further experiments [9]. The path of the beam is shown in Figure 2.4. It is generated at the
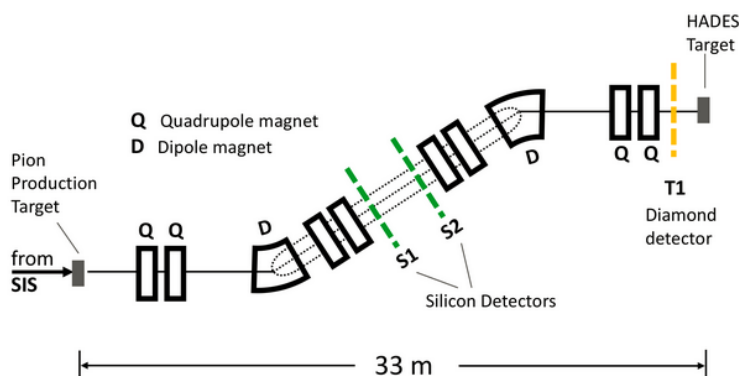
Figure 2.4: beam line of the pion beam [10].

production target on the left and traverses certain magnets. Dipole magnets provide the right deflection for negative charged pions and the combination of quadrupole magnets focus the beam. Because of the broad momentum resolution(Δp/p $\approx 10\%$) of the secondary pion beam, the pion tracker CERBEROS was built. The two silicon detectors are positioned 15 m before the HADES target and the hits in the two detectors allow a precise determination of the pion momentum within a resolution better than the demanded resolution of 0.5% [10].

Beam momentum	1.7 GeV/c
Target	$^{183.8}_{74}$W
Target diameter	12 mm
Number of segments	3
Distance between segment centers	18 mm
Length of segment	2.4 mm

Table 2.1: Information about the $\pi^- + $W run in July 2014.

Chapter 3

Basics about two Particle Correlations

3.1 Hanburry-Brown-Twiss-Effect

Robert Hanburry-Brown and Richard Q. Twiss were the first who measured the size of stellar sources by performing the so called intensity interferometry. They were able to determine the (angular) size of the star Sirius [11]. The method is based on the use of two detectors, which record signals from the same source (cp. Figure 3.1). The two particle coincidence yield $\langle n_{12} \rangle$ and the two single particle yields $\langle n_1 \rangle$,$\langle n_2 \rangle$ are measured and with these values a correlation function can be calculated with

$$C \;=\; \frac{\langle n_{12} \rangle}{\langle n_1 \rangle \langle n_2 \rangle}. \tag{3.1}$$

In contrast to the single particle yields, the coincidence yield includes the correlations [12].

Due to the indistinguishability of the photons, one cannot say which photon took which path (cp. Figure 3.1). To calculate the intensity at one detector the amplitudes for both paths have to be summed up. Assuming two spherical waves $\alpha \, \exp(ik \, |\vec{r} - \vec{r_a} + i\Phi_a)/|\vec{r} - \vec{r_a}|$ and $\beta \, \exp(ik \, |\vec{r} - \vec{r_b} + i\Phi_b)/|\vec{r} - \vec{r_b}|$, where α and β are the amplitudes, $\vec{r_i}$ are the emitting positions of the photons and the Φ_i are two random phases. The amplitude of both waves at detector 1 is given by

$$A_1 \;=\; \frac{1}{L} \left(\alpha \, exp(ikr_{1a} + i\Phi_a) + \beta \, exp(ikr_{1b} + i\Phi_b) \right). \tag{3.2}$$

r_{ij} represents the distance between detector i and the source of photon j. The random phases Φ_i disappear by averaging over them. The correlation is then given by

$$C(d) = \frac{\langle I_1 I_2 \rangle}{\langle I_1 \rangle \langle I_2 \rangle} = \frac{\langle A_1^2 A_2^2 \rangle}{\langle A_1^2 \rangle \langle A_2^2 \rangle} = 1 + 2 \frac{\left\langle |\alpha|^2 \right\rangle \left\langle |\beta|^2 \right\rangle}{\left(\left\langle |\alpha|^2 \right\rangle + \left\langle |\beta|^2 \right\rangle \right)} \cos(\vec{R} \cdot (\vec{k_2} - \vec{k_1})). \tag{3.3}$$

$\vec{k_i} \;=\; k\hat{r}_i$ represents the wave vector of the light seen by detector i. The interference term introduces the correlation signal, which dependents on the distance d of the
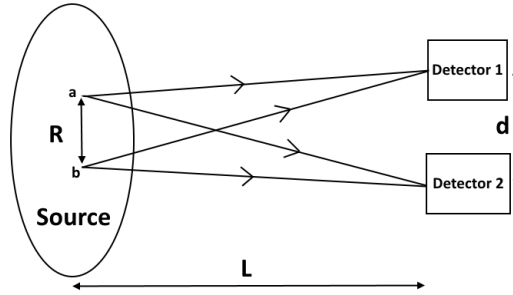
Figure 3.1: Schematic illustration of an intensity interferometry experiment. Two detectors record the signal from the same source. The coincidence yield and the two single particle yields can be used to calculate the correlation of the photons. The Function is given in Equation 3.1.

detectors. By varying $d = \frac{\lambda \cdot L}{R}$ one can gain information about the angular size R/L of the emitting system [13].

In 1960, Goldhaber *et al.*. showed that this method can not only be used for photons but also for identical pion pairs stemming from $p\bar{p}$-annihilation. They found that pions are preferably emitted at small relative angles. This could be explained with the symmetrization of the two pion wave function [14].

Bose-Einstein-Correlation

In quantum mechanics it is only possible to calculate probability distributions, which are given by the squares of the absolute value of the wave function and describe the system. The spin-statistics theorem states that a wave function of a system of identical bosons, particles with an integer spin, is always symmetric under exchange of two of them. Equation 3.4 gives an example for a symmetric wave function of a system with particle one in state a and particle two in state b. In contrast to the bosonic case the wave function of a system of identical fermions, particles with an half integer spin, is always antisymmetric (Equation 3.5).

$$\Psi_{1,2}^s(a,b) = \frac{1}{\sqrt{2}}\left(\Psi_1(a)\Psi_2(b) + \Psi_1(b)\Psi_2(a)\right) \tag{3.4}$$

$$\Psi_{1,2}^a(a,b) = \frac{1}{\sqrt{2}}\left(\Psi_1(a)\Psi_2(b) - \Psi_1(b)\Psi_2(a)\right) \tag{3.5}$$

As it can be seen in Equation 3.6, the probability for bosons to be found in the same state is two times higher than it would be expected for classical particles. This effect is named Bose-Einstein correlation. For fermions the probability for two particles

in the same state is zero, due to the Pauli principle. This implies that bosons with a small position and momentum difference, $\Delta x \cdot \Delta p \geq \frac{\hbar}{2}$ (Heisenberg's uncertainty principle), are more likely emitted pairwise. Furthermore it is possible to extract the spatial dimension of the particle source by investigating the momentum correlation.

$$\left|\Psi_{1,2}^{s}(a,a)\right|^2 \;=\; \left|\frac{2}{\sqrt{2}}\Psi_1(a)\Psi_2(a)\right|^2 \;=\; 2\left|\Psi_1(a)\right|^2\left|\Psi_2(a)\right|^2 \qquad (3.6)$$

$$\left|\Psi_{1,2}^{a}(a,a)\right|^2 \;=\; \left|\frac{1}{\sqrt{2}}\left(\Psi_1(a)\Psi_2(a)-\Psi_1(a)\Psi_2(a)\right)\right|^2 \;=\; 0 \qquad (3.7)$$

3.2 Correlation Function for Identical Pions

Pions are pseudo scalar particles with a spin of zero, and a system of two pions has a symmetrical wave function. The general wave function for such a system is given by Equation 3.4, where a and b are the two states of pion 1 and 2. The probability that both pions are found in the same state is given by Equation 3.6. On the grounds of Bose-Einstein-correlation, there is an enhancement of pions to be found in the same state. This correlation can be quantified by constructing a correlation function in momentum space to gain information about the particle emitting volume.

This means to take the ratio between the probability distribution of coincident momentum measurement and the two uncorrelated probabilities to measure these single momenta

$$C(p_1,p_2) \;=\; \frac{P(p_1,p_2)}{P(p_1)\cdot P(p_2)}. \qquad (3.8)$$

The coincident measurement $P(p_1,p_2)$ is given by the account of how often a particle with momentum p_1 is measured under the condition that a particle with momentum p_2 is measured, too. The uncorrelated values $P(p_i)$ are simply given by the probability to find a particle with momentum p_i. p_1 and p_2 are four vectors ($p^\mu = (E, p_x, p_y, p_z)$), which means that C depends on six different variables.

In order to reduce the degrees of freedom one constructs the correlation function as a function of the invariant relative momentum of the particles. This Lorentz invariant is given by Equation 4.7, where $\vec{p_1}$ and $\vec{p_2}$ are the three vectors of the momenta [13]

$$k \;=\; \frac{1}{2}\sqrt{(\vec{p_1}-\vec{p_2})^2 - (E_1-E_2)^2}. \qquad (3.9)$$

3.3 Three-dimensional Correlation Function

The analysis of the correlation strength differentially in beam and transverse directions reveals more detailed spatio-temporal information about the particle emitting

source. Usually the Pratt-Bertsch parametrization is used for this purpose in the so called "out-side-long" coordinates.

Pratt-Bertsch parametrization
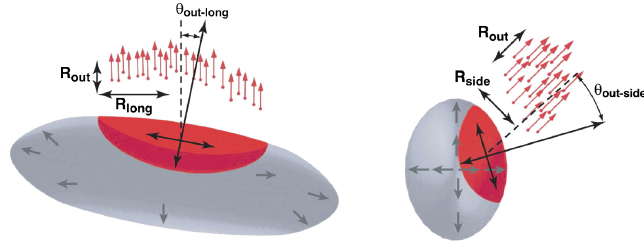
Lisa MA, et al. 2005.
Annu. Rev. Nucl. Part. Sci. 55:357–402

Figure 3.2: This figure illustrates the longitudinally co-moving coordinate system. In the left panel the beam axis is orientated horizontally. The same source distribution, but looking down the beam, is shown in the right pannel [15].

To analyze the correlation of two particles in three different directions, a longitudinally co-moving system is used. It is illustrated in Figure 3.2. With this coordinate system it is possible to compensate the beam momentum with a boost along the beam-axis such that $\vec{P}_z = 0$ when $\vec{P}$ is the momentum of the pair. The three axes are selected as follows. The long-axis is parallel to the beam-axis. The out-axis points along the total transverse momentum of the two pions and the side-axis is orthogonal on both. The relative momentum vector $\vec{k}$ in the LCMS is then decomposed in the three components parallel to the axes. The following equations show the results of the projections of the relative momentum vector in the LCMS. They are give in terms of the relative momentum $\vec{K} = \vec{p}_1 - \vec{p}_2$ and total momentum $\vec{P} = \vec{p}_1 + \vec{p}_2$ in the LCMS of the pair.

$$k_{out} = \frac{1}{2} \cdot \left| \frac{\vec{P}_t \cdot \vec{K}_t}{\left| \vec{P}_t \right|} \right| \tag{3.10}$$

$$k_{side} = \frac{1}{2} \cdot \left| \frac{\vec{K}_t \times \vec{P}_t}{\left| \vec{P}_t \right|} \right|_z \tag{3.11}$$

$$k_{long} = \frac{1}{2} \cdot \left| \vec{K}_z \right| \tag{3.12}$$

3.4 Bowler-Sinyukov parametrization

Bowler and Sinyukov *et al.* developed a parametrization for the correlation function of particles, which stem from a Gaussian source. They suggested to separate the coherent emission from the incoherent part, which contains the Bose-Einstein correlated particles. For this purpose the λ parameter is introduced. Since only the pion pairs, which are Bose-Einstein correlated, are considered to interact via Coulomb, the Coulomb term is multiplied to the incoherent part, too [16]. The resulting Equations are given in 3.13 for one dimension and in 3.14 for three dimensions. Afterwards, the important parameters are explained.

One-dimensional parametrization

For this analysis the one-dimensional correlation function will be parametrized with Equation 3.13. This representation is in accordance with the Bowler-Sinyukov parametrization. $(1 - \lambda)$ gives the coherent part which is not expected to act via Bose-Einstein correlation. The constants $\hbar$ and c are set to one.

$$C(k) \; = \; (1 - \lambda) + \lambda \cdot K_{Coul}(k) \cdot \left(1 + e^{-(2Rk)^2} \right). \tag{3.13}$$

Three - dimensional parametrization

A three-dimensional correlation function can be parametrized with the Bowler-Sinyukov procedure, too. One receives

$$C(k_o, k_s, k_l) \; = \; (1 - \lambda) + \lambda \cdot K_{Coul}(k, R) \cdot \left(1 + e^{-(2R_o k_o)^2 - (2R_s k_s)^2 - (2R_l k_l)^2} \right). \tag{3.14}$$

R_o, R_s and R_l give the three source radii respective to the LCM system.

3.4.1 The Lambda Parameter

The parameter λ indicates the percentage of pion pairs that show an Bose-Einstein enhancement and because of this reason are also considered to undergo Coulomb interaction. If there was no interaction at all ($\lambda = 0$) the correlation function would be equal to unity as expected, whereas $\lambda = 1$ means that all pairs are interacting and the maximal correlation would be C(0) = 2 [16]. A second possibility to describe the meaning of the λ parameter is that $\lambda = 1$ corresponds to a fully chaotic particle emitting source. If the λ parameter is smaller than unity, it corresponds to a partially coherent emitting source. By adding this parameter to the correlation function one takes into account the fact that the source is neither fully chaotic nor fully coherent [17]. Experimentally, a deviation of λ from unity can be caused by long lived

resonances, which decay a few thousand fm away from the source and are therefore not correlated with the other pions [15]. Another reason might be misidentified particles, which can not be Bose-Einstein correlated with the pions.

3.4.2 The Coulomb Contingent

The influence of the Coulomb interaction on the correlation strength of the pion pairs is taken into account by the factor $K_{Coul}(k, R)$. For identical pions, this interaction is repulsive. Assuming a point-like source the Coulomb influence is given by the Gamow factor

$$|\Psi(r \to 0)|^2 \;=\; K_{Coul}(\eta, 0) \;=\; \frac{2\pi\eta}{e^{2\pi\eta} - 1}. \tag{3.15}$$

With η given by the following Equation where μ is the reduced mass of the pion pair.

$$\eta \;=\; \frac{\mu e^2}{k}. \tag{3.16}$$

However, the point-like source is only an approximation and the pions are in reality emitted from a finite source. For this reason we use a factor for the Coulomb correction which is averaged over a Gaussian distribution with a source size R, the same as for the correlation signal. Figure 3.3 illustrates how the Coulomb factor changes for a finite source. The black curve represents the Gamow factor and the colored curves the Coulomb factor for a source with a finite radius. There is only a little change in the Coulomb correlation for small sources since deviations from the point-like approximation are small. However, for larger systems one would introduce a large error by neglecting the finite size of the emission zone. Since we expect no source radii bigger than 2 or 3 fm, the influence of the finite source size will stay small [15].
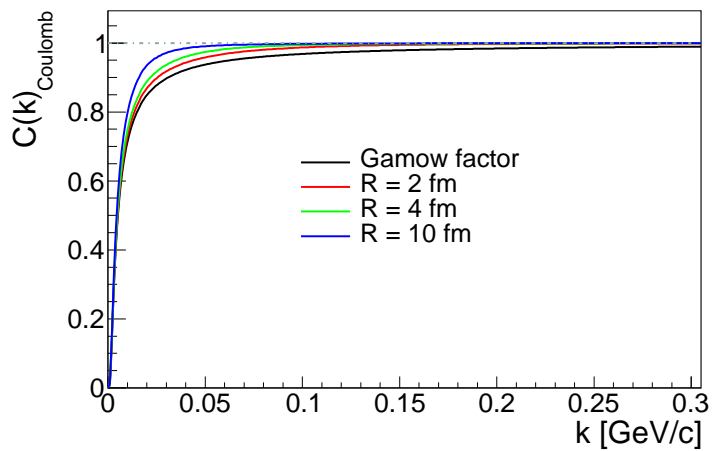
Figure 3.3: Coulomb factor for a point-like source (black) and sources with finite radii. The difference can be explained by the fact that pions stemming from a bigger source can have a bigger distance, which leads to a smaller influence of the Coulomb interaction.

Chapter 4

Analysis Methods

This chapter deals with the analysis of the experimental data. At first some selection criteria to receive pion samples are introduced. In Section 4.3 the construction of a one-dimensional correlation function and the necessary corrections are explained and calculated. Afterwards, the correlation in three dimensions is investigated.

4.1 Track Sorting

Every charged particle, which traverses the detector, leaves certain hit points. The Runge-Kutta method is used to find tracks, which fit to a combination of hit points. Sometimes it happens that two or more track candidates are fitted through the same hit. The best of these tracks has to be selected and the other ones are sorted out by the so called track sorter.
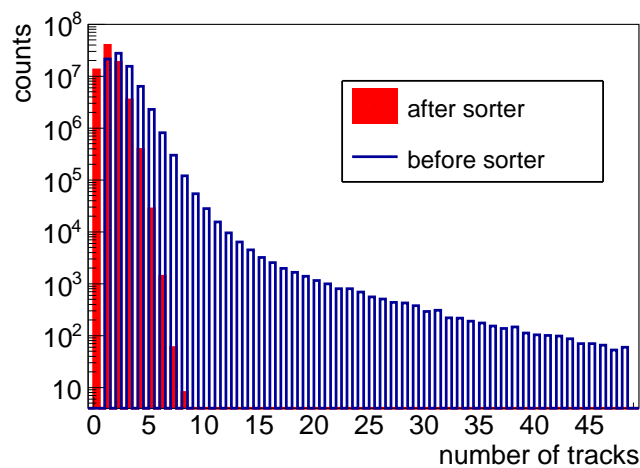
Figure 4.1: The blue bars show the multiplicities of the events before the track sorting. The red ones show the multiplicities after the track sorting. It is clearly visible that there are a lot of fake tracks, which can be rejected by the track sorter.

This is a tool of the Hydra analysis framework [18]. It tries to find the best track for a hit combination by using a selection criterion. In this case, the track has to consist of at least one hit in the inner and one in the outer MDC. It has to include a hit in the META system (cp. Section 2.1.3) and the χ^2 of the Runge-Kutta procedure has to be smaller than 1000. For the inner MDC χ^2 has to be bigger than 0 to reduce the amount of ghost tracks, which would induce an artificial positive correlation in the interesting region, and keep only unique tracks in the sample. A sorting of the tracks according to the product of the Runge-Kutta-χ^2 and the MetaMatch Quality is performed. Figure 4.2 illustrates that this tool is very effective. For all following graphics and analysis steps only the data after the application of the track sorter is used.

4.2 Particle identification

In the first step of the analysis we have to identify the pions. For this purpose we use several detector information. The first information is the energy loss provided by the Multi-wire drift chambers. Every charged particle, which traverses a medium, looses a certain amount of energy per distance via inelastic scattering with bound electrons of this medium. The amount of the energy loss depends on the charge, the momentum and especially on the mass of the traversing particle. This dependence is given by the famous Bethe-Bloch-formula [19]:

$$-\left\langle \frac{dE}{dx} \right\rangle = \frac{4\pi N_A r_e^2 m_e c^2 z^2 Z}{A\beta^2} \cdot \left(\ln\left(\frac{2m_e c^2 \beta^2 \gamma^2 T_{max}}{I^2} \right) - \beta^2 - \frac{\delta}{2} \right). \quad (4.1)$$

- A, Z : Mass and atomic number of the traversed medium

- m_e : rest mass of the electron

- r_e : Bohr radius

- z : charge number of the traversing particle

- N_A : Avogadro number

- I: mean excitation potential of the medium

- δ : density correction

- T_{max} : maximum of the transferred, kinetic energy

The dependence of the charge (z · e) is obvious and the dependence on the momentum and mass is given by $\beta\gamma = $ p/m. This means that particles with a certain mass and charge are expected to form different curves in a energy loss versus momentum spectrum, which allows to identify them.
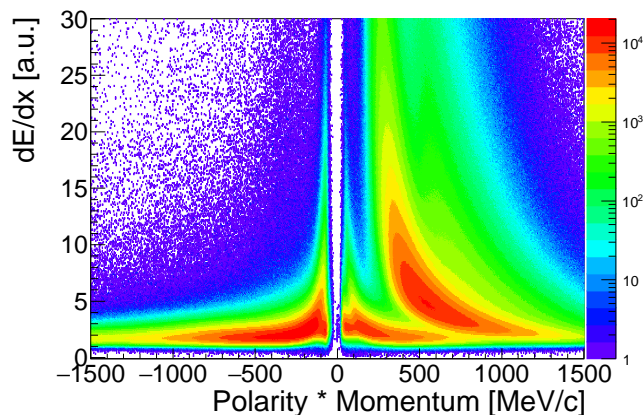
Figure 4.2: The energy loss measured by the MDC versus Polarity · Momentum is plotted. No preselection cuts are performed. On the left side one can see the band of negative pions. The lowest band at small momenta on the right side belongs to the positive pions. Above them the protons can be seen. The slightly visible band about the protons belongs to deuterons.

4.2.1 Particle Identification with the MDC

The MDCs provide an information about how much energy a measured particle looses by traversing a certain distance. One can plot this value for every track versus the product of momentum and polarity. The resulting histogram is shown in Figure 4.2. The bands for negative pions on the left and for positive pions, as well as for protons and also deuterons on the right are clearly visible. The pions, the lightest of these particles loose the fewest energy at low momenta. Above the π^+ band a broad proton area can be seen. The upmost band belongs to deuterons. Because the energy loss depends only on the mass and momentum of the traversing pions, particles with similar mass and momentum like muons deposit the same energy in the detector. For this reason we use additional information from other detector components to avoid this misidentification, which will be shown in the next Section 4.2.2.

Within this thesis, a method to construct particle identification cuts with the energy loss and momentum information by using experimental data, is developed. To perform this cut construction, we have to preselect the pions in which we are interested. For this reason we introduce a loose cut on the pion mass (measured by the time of flight detectors) in a window of $m_\pi \pm 100$ MeV/c^2 to reduce the contamination coming from protons and deuterons. Otherwise the fitting does not work. The resulting distribution can be seen in Figure 4.3. This mass interval is only used to build the graphical cuts. In the next Section 4.2.2 we discuss how to include the mass information for particle identification.
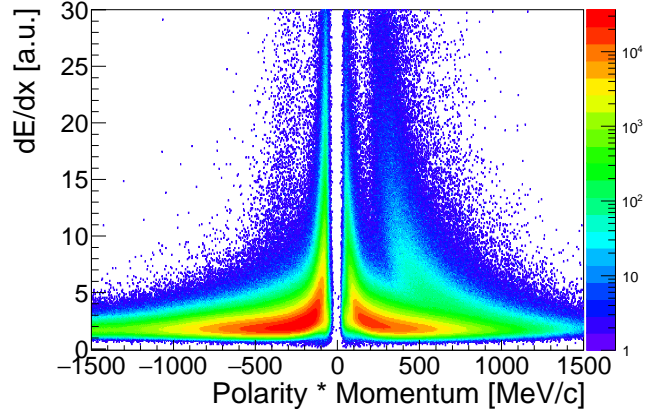
Figure 4.3: The energy loss measured by the MDC versus Polarity · Momentum is plotted. All tracks within the window $m_\pi \pm 100$ MeV/c^2 are used to generate this histogram. The amount of protons and deuterons is decreased.

The histogram shown in Figure 4.3 is divided into momentum slices of 30 MeV/c, which are then projected on the dE/dx-axis and fitted with the numerical form of Equation 4.2 with mean$_{\text{Landau}}$, σ_{Landau} and σ_{Gaus} as fit parameters.

$$f(x) = \int \text{Landau}_{\sigma_L, mean_L}(x) \, \text{Gauss}_{\sigma_G}(x - x') \, dx'. \tag{4.2}$$

The Landau is chosen, because the distribution is asymmetric as it can be seen in Figure 4.4(b). The convolution with the Gaussian stands for the finite resolution of the experimental data. Figure 4.4(b) shows an example for a fitted momentum slice. The dashed red lines show the range $3.5 \cdot (0.5 \cdot (\sigma_G + \sigma_L))$ around the mean mean$_L$. Everything within this region is treated as pion. However, at some slices at higher momenta, the fit fails due to too few pions. At the first slice where this happen, we stop the procedure. That is the reason why the cuts don't include the whole momentum range. The resulting cuts with the data they are fitted with is shown in Figure 4.5(a) and the cuts without a mass preselection on the pions is shown in Figure 4.5(b). As one can see the fit of the positive charged pions already stops at a momentum of 600 MeV/c. This is due to the fact that at higher momenta the cut would overlap with the proton band, which would lead to misidentification, that we want to exclude. In the Appendix A.1, A.2, A.3 and A.4 the stability of this procedure is shown. Some example slices are fitted for the data of the different beam days and the resulting means and sigma are compared. The procedure seems to produce stable results.

(a)　　　　　　　　　　　　　　　(b)
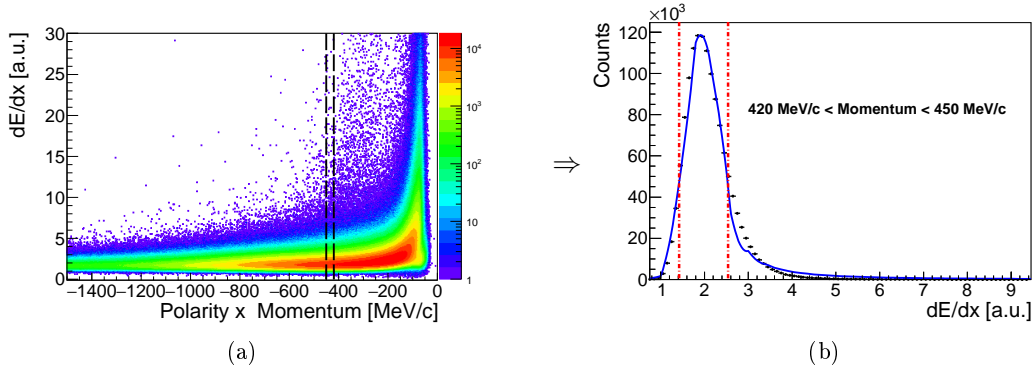
Figure 4.4: One example for the projected momentum slices, which are fitted with a convolution of a Gaussian and a Landau function. As a representative to illustrate the developed method, a projected energy loss within a momentum interval of 420 - 450 MeV/c is shown for negative pions. The preselection on pions by cutting on the mass information provided by the TOF/RPC is made ($m \in m_\pi \pm 100$ MeV/c^2). This distribution is fitted with Equation 4.2, which is displayed as blue solid line. The dashed red lines give the 3.5 sigma environment. Everything inside these lines is treated as pion.

(a)　　　　　　　　　　　　　　　(b)
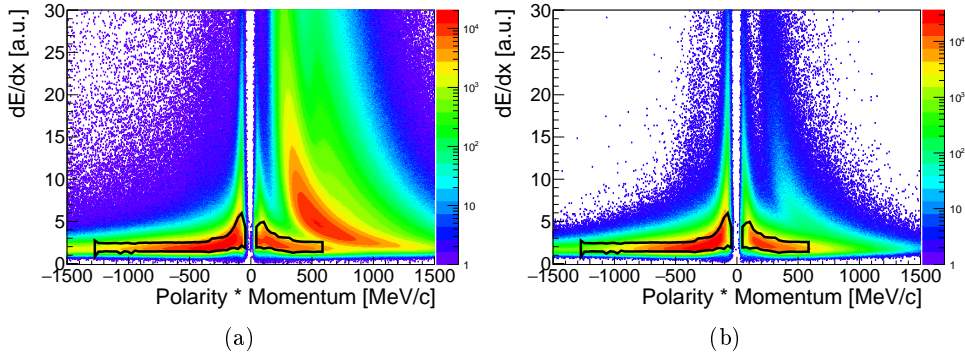
Figure 4.5: The energy loss measured by the MDCs, is plotted versus Polarity · Momentum. In the Figure 4.5(a) the pions are preselected within $m_\pi \pm 100$ MeV/c^2,which is necessary to fit the distribution. On the right no preselection on the mass was made. In both plots the graphical cuts for pion identification are displayed as black solid lines.

4.2.2 Particle Identification with TOF and RPC

Additionally to the identification via the MDC energy loss information we examine the use of the time of flight signal provided by the TOF and RPC components. As we will see in this section it is useful to reject electron contamination. Due to their different time resolution the following method is developed for TOF and RPC separately. Both detectors provide an information about $\beta = \frac{v}{c}$ for every track. This value can be plotted against the momentum.

$$\beta(p) = \frac{p}{E} = \frac{p}{\sqrt{p^2 + m^2}} \tag{4.3}$$

Because of Equation 4.3 different particle species form bands, which can be distinguished due to the particle mass. Figure 4.7(a) and 4.7(b) show the distribution of β versus the product of momentum and polarity under the condition that the particle lays within the energy loss cut (MDC) described in section 4.2.1. They also show the cuts, which are explained within this section. It is clearly visible in Figure 4.7 that beside the two pion bands, there are still two peaks with a rather small momentum, but nearly the speed of light. Based on their position in this plot, they can be identified as electrons and positrons. It is obvious that the energy loss cut alone is not able to reject electrons and that we have to introduce a second PID cut to reach the aim of a clean pion sample.

To obtain a second graphical cut from experimental data, the β versus momentum plot is also divided into momentum slices analogously as for the energy loss. Due to the electron contamination, we have to use a preselection cut again, to keep our fitting procedure possible. This time we don't have to dispose protons, since they are rejected by the MDC. We choose an upper limit of $m_\pi + 200$ MeV/c^2, but a lower limit of $m_\pi - 75$ MeV/c^2 to dispose the electrons and make this fitting possible. Since the second preselection excludes very low masses, it introduces a hole around $\beta = 1$. Due to this hole in the pion band, we cannot fit the the whole pion distribution, but take the more physical side with $\beta < 1$. In this case we use 35 slices in a region of 0 - 800 MeV/c (22.9 MeV/c per slice), which are fitted only with a Gaussian, because the projected distribution has to be stopped at $\beta = 1$ as it was explained before, which makes the asyymetric part disappear. A example slice is given in Figure 4.6(d). For low momenta, the distribution cannot be fitted anymore because it becomes parallel to the momentum slices (cp. Figure 4.7). For this region we use β slices and project them on the momentum axis. The range of $0.2 < \beta < 1$ is divided into 20 beta slices of $\Delta\beta = 0.04$. These slices are fitted with Equation 4.2, a convolution of a Landau distribution and a Gaussian. Similar to the MDC cut, the Landau is used to describe the asymmetric form and the Gaussian describes the finite resolution of the data. As it can be seen in Figure 4.6(b) the fit does not converge as good as for the MDC data, but the resulting cut describes the form of

the pion band (cp. Figure 4.7).

For the momentum slices we choose an area of 1.5 σ around the mean and for the beta slices we choose $2.5 \cdot (0.5 \cdot (\sigma_g + \sigma_l))$. The areas are marked with the dashed red lines in Figure 4.6(b) and 4.6(d). The two cuts for both slicing directions are separately combined and subsequently the incorporation of both is taken for the particle identification and can be seen in Figure 4.7(a) and 4.7(b).

(a)

(b)

(c)

(d)
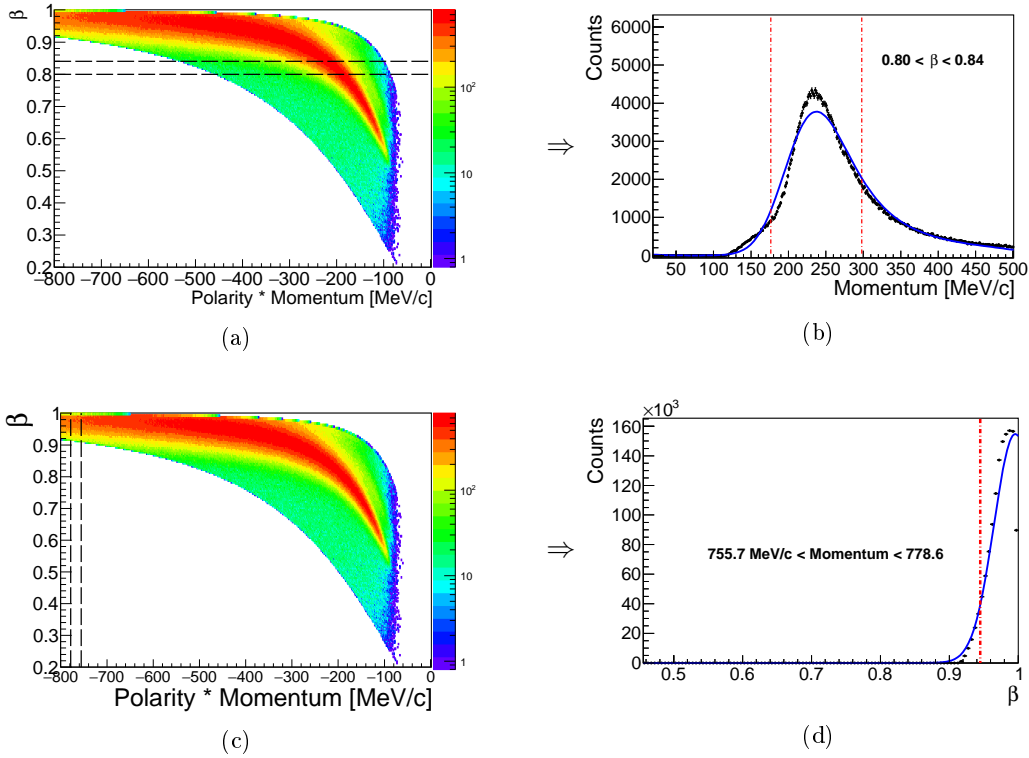
Figure 4.6: One example for the projected β slices (RPC) in (a) and (b), which are fitted with a convolution of a Gaussian and a Landau function and one example for the projected momentum slices in (c) and (d), which are fitted with a Gaussian are shown. Both representatives shall illustrate the developed method. The preselection on pions by cutting on the mass of $m_\pi - 75$ MeV/c$^2 < m < m_\pi + 200$ MeV/c^2 information is made again to make a fit possible. The fitted functions are shown as blue solid lines and everything within the dashed red lines is taken as pion.

(a) This plot contains the PID cut, calculated for the TOF measurements.

(b) This plot contains the PID cut, calculated for the RPC measurements.
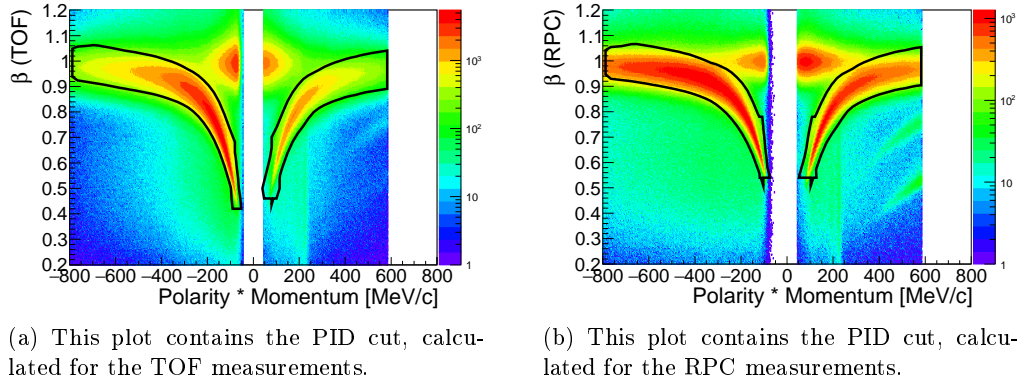
Figure 4.7: $\beta = \frac{v}{c}$, measured by the TOF on the left and by RPC on the right, is plotted against Polarity · Momentum. Both plots contain only tracks which fulfill the MDC-PID-cut. The black curves describe the graphical cuts, which are used for PID.

To have an overview all particle identification cuts are summarized in Table 4.1.

	MDC vertical	**TOF + RPC** vertical	**TOF + RPC** horizontal
Range	0 - 1500 MeV/c	0 - 800 MeV/c	0.2 - 1
Fragmentation	50 momentum slices of 30 MeV/c	35 momentum slices of 22.9 MeV/c	20 β slices of 0.04
Fit function	Landau x Gaussian	Gaussian	Landau x Gaussian
Mean	$mean_l$	$mean_g$	$mean_l$
width σ	$3.5 \cdot 0.5(\sigma_l + \sigma_g)$	$1.5 \cdot \sigma_g$	$2.5 \cdot 0.5(\sigma_l + \sigma_g)$

Table 4.1: These are all important information for the pion identification cuts. The range is divided into a certain amount of slices. These slices are fitted with the fit function and the fitted means $\pm \sigma$ are than combined the two dimensional cuts.

4.2.3 Purity Estimation

Two different detector information are used to identify the pions. It's possible to quantify the quality of these graphical cuts. For this purpose we use the mass information provided by the TOF and RPC detectors. Plotting the mass of the identified pions versus the product of polarity and momentum one can still distinguish between the pion band (139.57 MeV/c^2) and the muon band (105.66 MeV/c^2) below. An example for the positive pions and the RPC data is shown in Figure 4.8. Figure 4.8(a) contains all pion candidates after the appliance of the MDC cut, but without the graphical β cut. In the Figure 4.8(c) the identified pions after MDC and RPC cut are shown. All graphics are also given for the TOF data in the Appendix. The black lines in the mass spectra indicate that the histogram is divided into momentum slices of 5 MeV/c. These slices are projected to the mass axis and then fitted with a combination of three Gaussians, one for the pions, one for the electrons/positrons and one for the muons. This procedure can be seen in Figure 4.8(b) and 4.8(d). The signal is given by the integral over the Gaussian which describes the pions and signal plus background is given by an integral over the whole distribution, since this is what we identify as pions. The Purity can now be calculated by

$$Purity \ = \ \frac{Signal}{Signal + Background}.\qquad(4.4)$$

Unfortunately we can only give evidence about the purity in a region of 50 - 200 MeV/c, because for higher momenta the pion band gets so brought that it is not possible to distinguish between the pion and the muon peak. The purity after the MDC cut is plotted as red dots, whereas the pions after the MDC and β cuts are plotted as blue dots in Figure 4.9 Applying the second PID cut (blue) improves the pion samples in all four cases (Figure 4.9). However, one has to consider that these plots give only a rough estimate of the purity, since the muons merge with the pions for higher momenta although the purity goes to one. Moreover the fit could be repeated with an additional function for the background to improve it for the slices where it obviously did not work. One can recognize these slices as outlier points in Figure 4.9. Additionally this would improve the fit for the TOF data. It can be seen in Figure A.7(a) that the pion peak for TOF data is underestimated which leads to an underestimated purity. However, the trend, that we have a much better purity after applying the second PID cut is clearly visible. An observation looking at the purity plots is that the purity of the positive pions (right figures) is slightly better than the one for the negative pions.

(a)

(b)

(c)

(d)
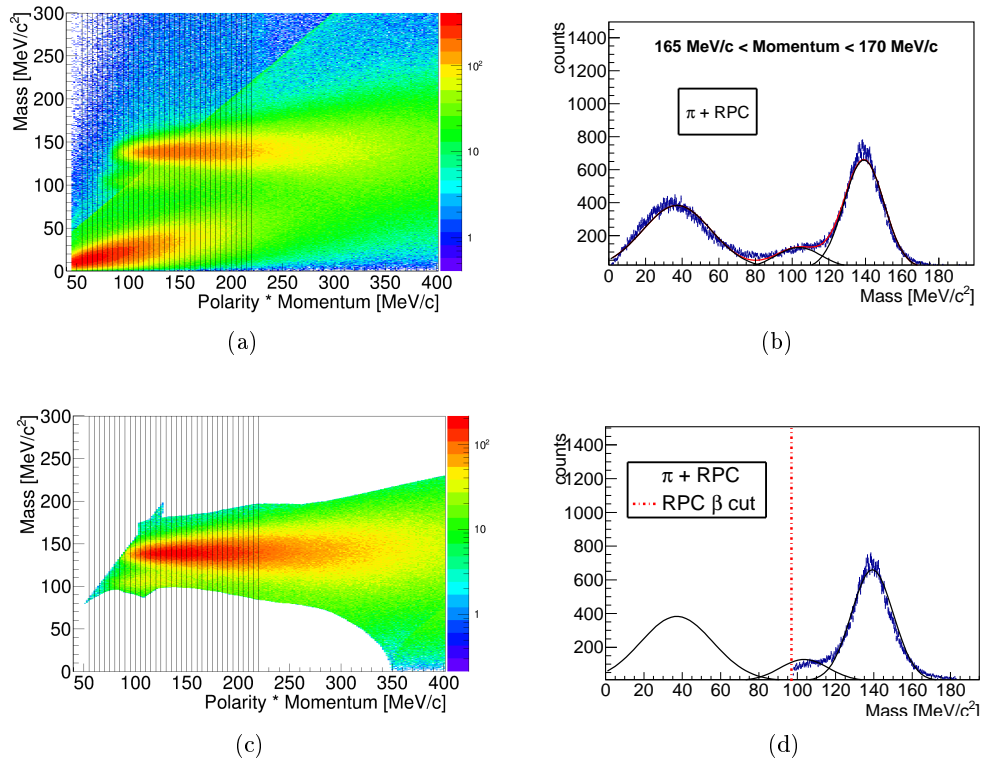
Figure 4.8: The mass versus momentum distribution after the two steps (MDC cut, MDC + RPC cut) of the particle identification are plotted for positive polarity and the RPC data. The histograms are divided into momentum slices of 5 MeV/c by the black lines. In the right plots one slice (165 MeV/c - 170 MeV/c) is shown. The blue data points are fitted with three Gaussian. The right Gaussian fits the pion peak. In the lower, right plot the red line indicates the additional β-cut. The improvement is clearly visible.
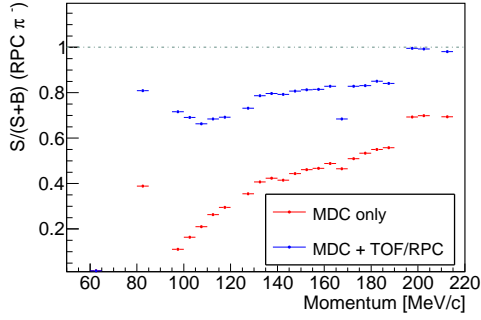
(a) Purity of the negative pions measured with the RPC for different momentum slices.
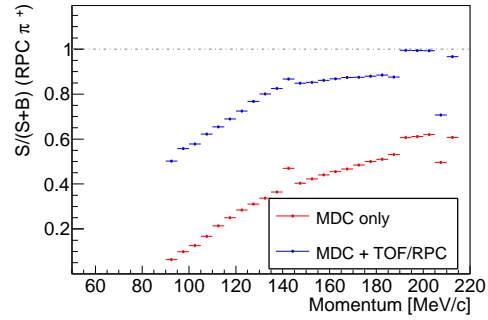
(b) Purity of the positive pions measured with the RPC for different momentum slices.
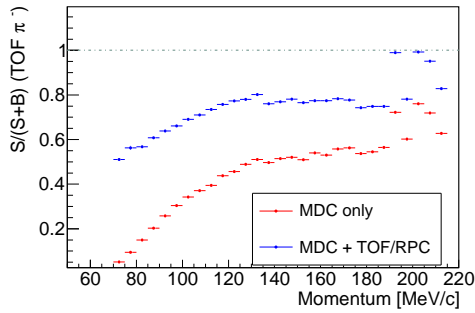
(c) Purity of the negative pions measured with the TOF for different momentum slices.
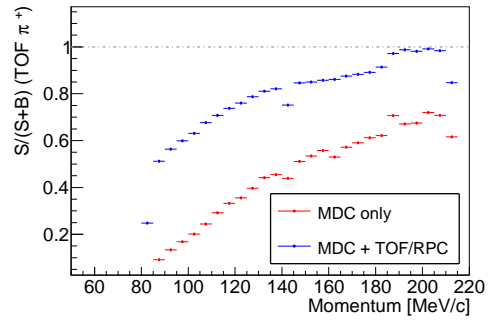
(d) Purity of the positive pions measured with the TOF for different momentum slices.

Figure 4.9: Purity estimation for the pions after the MDC cut (red) and after both, MDC + TOF/RPC cut, (blue), for different momentum slices are shown. The left figures show the purity estimation for π^- and the right ones for π^+. The upper Figures show the RPC data and the lower ones the TOF data. All slices were fitted with three Gaussians and signal and background yield was determined by these fits.

4.3 One-dimensional Correlation function and Corrections for π^+ and π^-

In order to calculate the correlation function a certain set of particles is prepared. To select the pions we used the PID information from the MDCs and the TOF/RPC system. The graphical cuts were shown in the previous section. To select only primary pions we employ also a cut on the z component of the primary vertex (-79 cm $<$ z $<$ 11 cm). With these cuts the pions for the correlation analysis are selected.

4.3.1 Construction of the Correlation Function

To obtain the experimental correlation function the distribution of the relative momentum of two pions from the same event is divided by the distribution of the relative momentum of two pions from different events, which are by construction not correlated. This method makes sure that only the correlation between the two investigated particles remains

$$C(k) \;=\; N \cdot \frac{A_{same}(k)}{B_{mixed}(k)} \tag{4.5}$$

$$N \;=\; \frac{\int_{150\ MeV/c}^{300\ MeV/c} B_{mixed}(k)\,\mathrm{d}k}{\int_{150\ MeV/c}^{300\ MeV/c} A_{same}(k)\,\mathrm{d}k}. \tag{4.6}$$

This connection is given by Equation 4.5, where k is the half of the absolute value of the momentum difference of both pions in their center of mass frame. The calculation of this quantity is given by

$$k \;=\; \frac{1}{2}\sqrt{(\vec{p_1} - \vec{p_2})^2 - (E_1 - E_2)^2} \;=\; \frac{1}{2}\sqrt{(\vec{p_1}_{CMS} - \vec{p_2}_{CMS})^2} \;=\; |\vec{p_1}_{CMS}| \;=\; |\vec{p_2}_{CMS}|. \tag{4.7}$$

N is a normalization factor, which is given by Equation 4.6. The momentum interval (150 MeV/c - 300 MeV/c) is chosen outside of the correlation region, where the correlation function is expected to be one. Events which are mixed are binned in their multiplicity to mix events which have similar kinematic structure and additionally the acceptance of the detector should be similar, which is taken into account by mixing only events stemming from a similar z-vertex position. In this case the events are classified in three multiplicity and five z-vertex position classes, which are shown in Table 4.2 and 4.3.

Multiplicity class	Multiplicity (charged particles)
1	0 - 2
2	3 - 5
3	6 - 8

Table 4.2: Multiplicity (charged particles) classes for the event mixing

Vertex class	z position of the event vertex [cm]		
1	-79	-	-61
2	-61	-	-43
3	-43	-	-25
4	-25	-	-7
5	-7	-	11

Table 4.3: z - position classes for the event mixing

We don't have to take into account higher multiplicities than 8, because after the track sorting there are no events with a higher multiplicity than that. Also the vertex class order is reasonable, as it can be seen in Figure 4.10. The mixing bins, displayed by the black lines, make sure that the mixed events stem from similar target regions. Every event is stored according to the z-vertex and multiplicity information. When enough events are stored for a certain configuration the events are mixed.
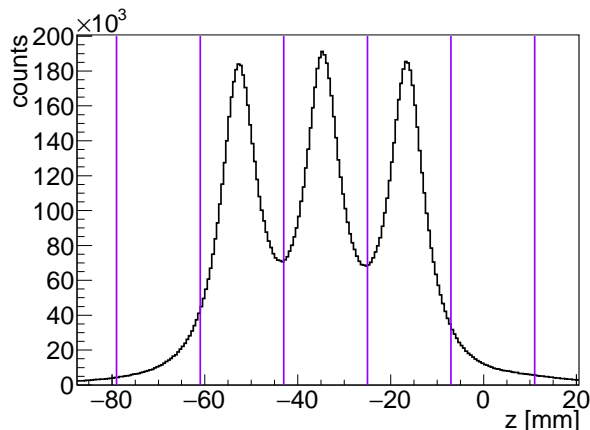
Figure 4.10: Primary z-vertex distribution of a subsample of all the events is shown. The target geometry of three tungsten targets is clearly visible and the purple lines mark the different vertex classes which are used for the particle mixing.

After performing this for all particles which are identified as pions, we get 1.148.386 real π^- pairs and 8.920.792 mixed pairs. The statistics for π^+ is much smaller with 92.273 real pairs and 613.059 mixed pair. The main reason for this is that we deal with an π^- beam, which means there is an excess of negative charge as initial condition for reactions with neutrons. In the case of a reaction with a proton there is no charge excess, but due to the conservation of the baryon number we have to

remain with either a positive baryon (proton) and at least one negative particle (e.g. π^-) or a neutral baryon (neutron) an something charge neutral (e.g. a $\pi^+\pi^-$ pair). Another point to consider is that positive charged pions with an momentum higher than 600 MeV/c are always rejected due to the MDC PID-cut.

In Figure 4.11(a) and 4.11(b) the first results for the correlation functions are shown. Unfortunately the long range behavior looks not like expected. In general one would expect a flat distribution without correlations. Especially for the negative pions it shows a peak at 500 MeV/c relative momentum. Apparently the mixed event distribution fails for higher momenta. This could be caused by additional correlations through the energy and momentum conservation and has to be studied in the future. However we are interested in the region of small relative momenta to gain information about the particle emitting source and this region looks like expected for both pion types.

(a) neative pion pairs   (b) positive pion pairs
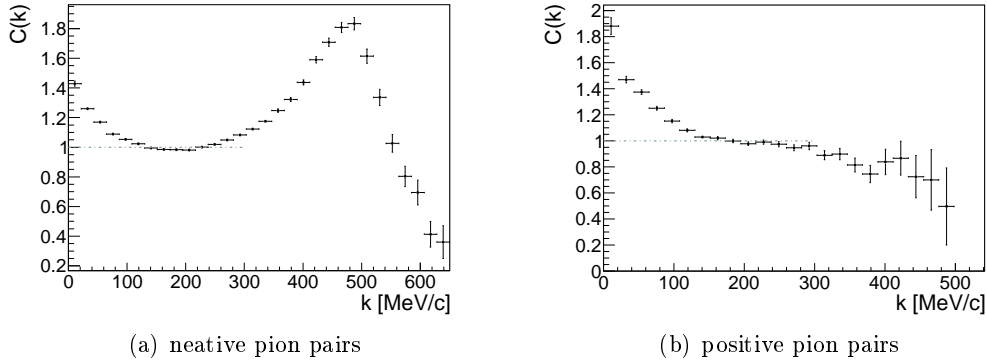
Figure 4.11: Correlation functions for the identical pion pairs. There are still some problems with the long range correlations, especially for the negative pions. However, both curves show the expected correlation at low relative momenta.

4.3.2 Corrections

In order to extract information about the real correlation between the pions from the correlation functions, a few corrections have to be done.

Close track efficiency

Imagine two pions, which fly very close to each other into the detector, the detector can't resolve them anymore and their hit points are combined to one track. This so called track merging leads to a suppression of measured pion pairs at small relative momenta. Since we use different tracks by construction for the mixed event method,

they are never merged. The fact that this lack of pairs only exists for $A_{same}(k)$ introduces a fake anti-correlation to the measured correlation function. In order to correct this, one can reject pairs with too small relative angles for the same and mixed event distribution. The easiest way to perform this correction is to look at at a two-dimensional relative, angular distribution of the pion pairs. To every particle track a polar angle Θ and a azimuthal angle Φ is assigned, when it is detected. Both angles are calculated in respect to the beam axis. The difference of the polar angles of both tracks ($\Delta\Theta$) is plotted against the azimuthal angle difference ($\Delta\Phi \cdot 0.5(\sin(\Theta_{pion1}) + \sin(\Theta_{pion2}))$). If one imagines two pions with a certain $\Delta\Phi$ flying at Θ_a into the detector, their relative distance is different compared to another pair hitting the detector at a different angle Θ_b but identical $\Delta\Phi$. This implies that we have to scale $\Delta\Phi$ with $\sin\Theta$. To compensate the difference both pions might have in polar direction we scale with the mean of $\sin\Theta$ of both pion. In Figure 4.12 these distributions are shown for negative pion pairs from the same event (Figure 4.12(a)) and from mixed events (Figure 4.12(b)).

One can clearly see that the track merging only affects the histogram for same events. Figure 4.12(c) represents the logarithmic plotted ratio of both distributions. With rejecting an amount of track pairs within this region, the fake anti-correlation can be reduced. The more merged tracks are rejected, the higher becomes the value of the correlation function at small relative momenta. As soon as the whole suppression region is rejected, the form of the correlation stays constant. A bigger cut would only reduce the statistic. Different radii and eccentricities were tested to cut the merged tracks out of the sample and the best combination of reducing the fake correlation and keeping as much statistics as possible is chosen. The best combinations are given in Equation 4.8 and 4.9. In the case of negative pions the angular cut is shown as black ellipse in Figure 4.12(c). For the positive pions the suppression is not visible in the angular distribution, due to the worse statistic, and the size of the cut is adapted by exploring the behavior of the correlation function by increasing the angular cut range. When the correlation signal height keeps constant the optimal cut range is found. The angular distributions are shown in the Appendix in Figure A.5.

In Figure 4.13 the correlations for small relative momenta are shown before (black) and after (red) the cut in the angular distribution.
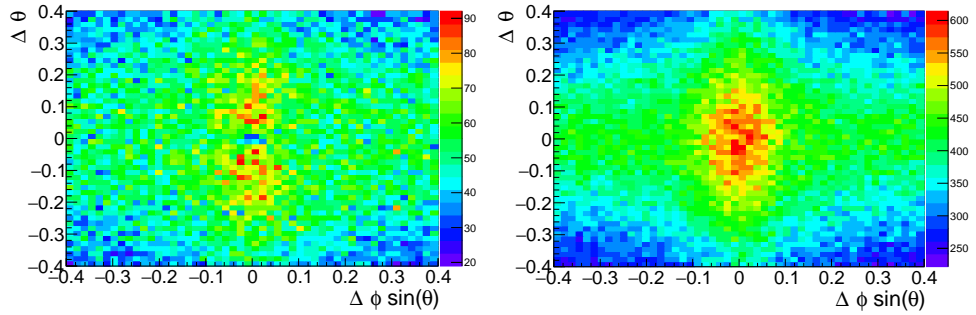
(a) angular distribution for negative pion pairs from the same event.

(b) angular distribution for negative pion pairs from mixed events.
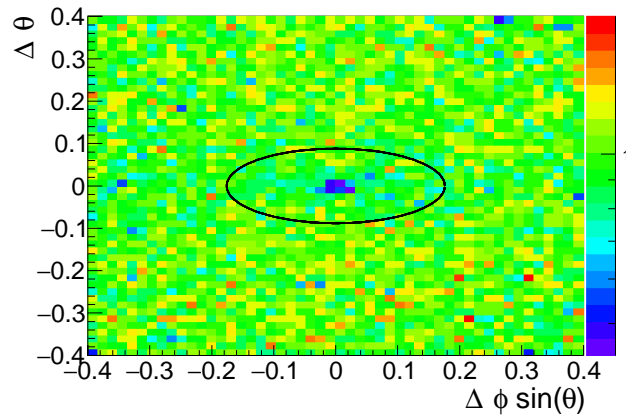
(c) The logarithmic ratio of distribution (a) and distribution (b) makes the lack clearly visible.

Figure 4.12: The relative, angular distributions is shown for negative pion pairs from the same event (a) and mixed events (b). The lower plot shows the ratio of both. The suppressing of too close pairs through track merging is visible. The trackswithin the black ellipse are rejected to correct the correlation function.

(a) Correlation function for π^- with (red) and without (black) angular cut.

(b) Correlation function for π^+ with (red) and without (black) angular cut.
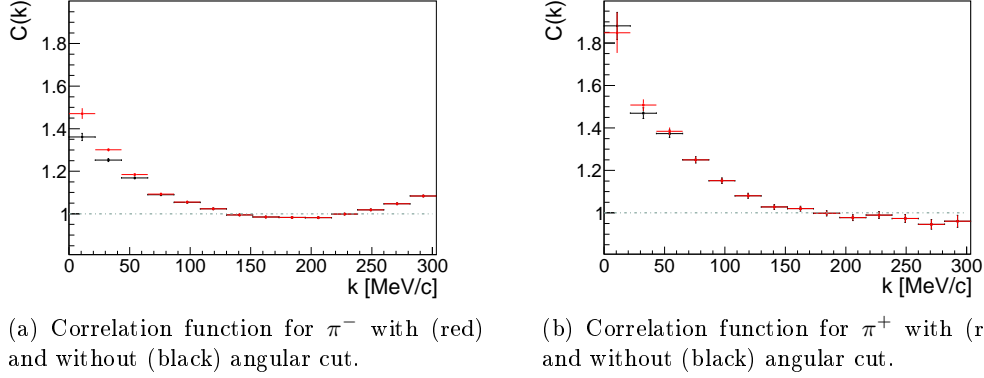
Figure 4.13: Correlation functions with(red) and without(black) cut on the angular distribution to reject merged tracks. The rise, caused by rejecting the merged tracks, is maximized for the shown curves.

The used cuts for negative and positive pions are given by

$$\pi^- : \qquad \sqrt{\left(\frac{\Delta\Phi \cdot 0.5(\sin(\Theta_1) + \sin(\Theta_2))}{10.08°}\right)^2 + \left(\frac{\Delta\Theta}{5.04°}\right)^2} > 1 \qquad (4.8)$$

$$\pi^+ : \qquad \sqrt{\left(\frac{\Delta\Phi \cdot 0.5(\sin(\Theta_1) + \sin(\Theta_2))}{11.45°}\right)^2 + \left(\frac{\Delta\Theta}{5.73°}\right)^2} > 1 \qquad (4.9)$$

Comparison to Simulation

Furthermore the result can be compared to simulated data. As an event generator we used the UrQMD simulation model [20]. Because the correlation effects are not simulated, the correlation function is expected to stay flat. But due to the simulated detector resolution the tracks are merged and we see an anti-correlation also for the simulated data. Assuming our angular cut removes all the merged tracks, the simulation should stay one after disposing this cut. The result of simulated correlation function before and after the angular cut is shown for negative pions in Figure 4.14.

(a) Correlation functions before the angular cut for negative pions.

(b) Correlation functions after the angular cut for negative pions.
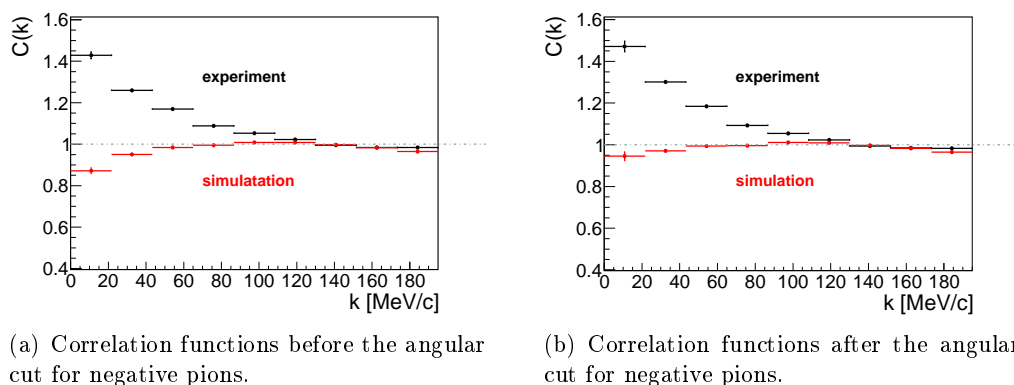
Figure 4.14: The experimental (black) and the simulated (red) correlation functions for negative pions are shown before (left) and after (right) the angular cut. One can see that the anti-correlation for the simulated data disappears nearly completely after the angular cut.

It is clearly visible that the angular cut reduces the anti-correlation for the simulated data. Unless it becomes not exactly one in the first bin, we reduce the most merged tracks. It should be mentioned that this result for the simulated data is not very stable under changes in the particle identification. The same approach was disposed to the positive pions, but unfortunately in this range the simulated data does not describe the expected behavior, as it is visible in Figure 4.15. The simulated correlation function does not show the expected behavior but a positive correlation before and after the angular cut.

(a) Correlation functions before the angular cut for positive pions.

(b) Correlation functions after the angular cut for positive pions.
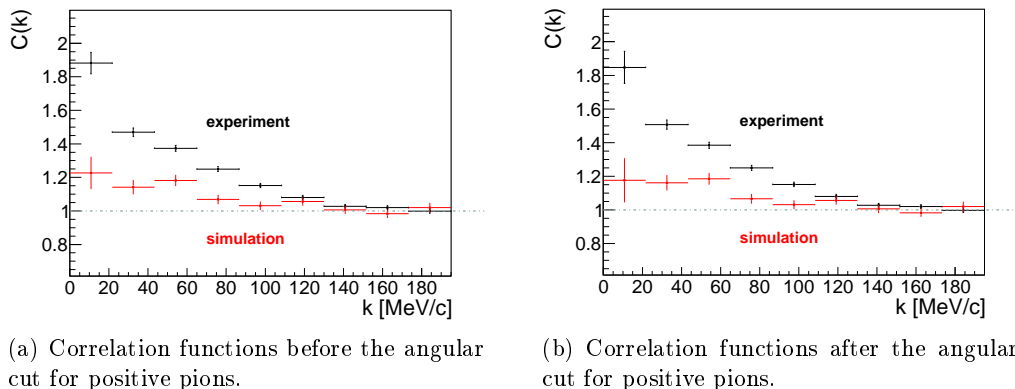
Figure 4.15: The experimental (black) and the simulated (red) correlation functions for positive pions are shown are shown before (left) and after (right) the angular cut. Unfortunately the simulated correlation function does not show the expected behavior at all.

In conclusion the simulated data shows that the angular cut has the right effect for negative pions. However the simulation has to be improved because it doesn't give physical results for the positive pions and is still very unstable for the negative ones.

Coulomb interaction

Since pions are charged particles, their Coulomb interaction has to be taken into account. We analyze correlations between identical pion pairs, whose Coulomb interaction is repulsive due to their identical charge. This has the effect that the correlation function is coulomb-suppressed for small relative momenta. This has to be considered by analyzing the correlation. As it was mentioned in section 3.2 the one-dimensional correlation function can be described with the following equation

$$C(k) \; = \; 1 \; - \; \lambda + \lambda \cdot K_{Coulomb}(k, R) \cdot \left(1 + e^{-(2kR)^2} \right). \qquad (4.10)$$

The influence of such a $K_{Coulomb}(k, R)$ factor is illustrated in Figure 3.3. The problem is that the Coulomb correction itself depends on the source radius which we want to extract. At the beginning we use the point-like approximation which results in the Gamow factor (R=0) for the Coulomb interaction. This approach is fitted to the experimental correlation function and the fit result for R is used to calculate the Coulomb factor for a source with this radius. Now this new Coulomb factor is inserted into Equation 4.10 and the fitting procedure is repeated. This iterative approach is repeated until the result for the radius stays constant. In the end the

result is given by $R_{\pi^-} = 1.40$ fm and $R_{\pi^+} = 1.22$ fm and the Lambda parameters $\lambda_{\pi^-} = 0.31$ and $\lambda_{\pi^+} = 0.71$. The fitted correlation functions for these parameters are shown in Figure 4.16.
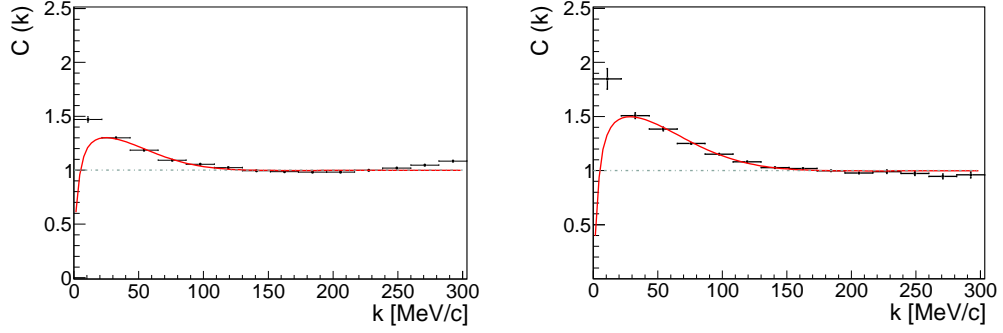
(a) Correlation function for π^- with full Coulomb correction.

(b) Correlation function for π^+ with full Coulomb correction.

Figure 4.16: The correlation functions are fitted with Equation 4.10. The fit results are given by $R_{\pi^-} = 1.40$ fm and $\lambda_{\pi^-} = 0.31$ for the left plot and by $R_{\pi^+} = 1.22$ fm and $\lambda_{\pi^+} = 0.71$ for the right one.

The strong interaction between two pions is so small that it can be neglected for this analysis [16].

4.4 Experimental Three-dimensional Correlation Function

Although the one-dimensional correlation function contains a lot of information, we are interested in the differences of the correlation strength in beam and transverse direction. For this purpose one can create a three-dimensional correlation function. For the following analysis only pion pairs within all PID-cuts and with sufficient angular distance (cp. Equation 4.8 and 4.9) are used.

4.4.1 Projection in the Three Dimensions

The one-dimensional correlation function depends on the invariant relative momentum of two pions in their center of mass system. For the three-dimensional analysis the longitudinally co-moving system, described in Section 3.3 is used. The next steps are performed for the negative and also for the positive charged pion sample analogously but only described once. A three-dimensional histograms is filled with k_{out}, k_{side} and k_{long}. Afterwards the histogram is projected onto every axis once. The projection is always performed in the interval 0 - 20 MeV/c at the other two axes, since we are interested in the correlations at small relative momenta. To calculate for example the distribution for k_{out} all entries within $k_{side}, k_{long} \leq 20$ MeV/c are projected on the out-axis to get an one-dimensional histogram. This procedure is performed for same and mixed events separately, which gives three same event - mixed event histogram pairs. These historams can be treated like the ones for the one-dimensional correlation function. Equation 4.5 is used and the normalization is performed between 150 MeV/c and 300 MeV/c because in this area no correlations are assumed. The resulting correlations are shown in Figure 4.17.

4.4.2 Three-dimensional Fit

In order to quantify the differences in the correlation signals, the three resulting histograms are fitted with Equation 3.14 for every direction simultaneously in a range of 0 - 150 MeV/c where the correlation is expected. For the Coulomb factor, the different results for π^- and π^+ from the one dimensional, iterative fitting are used (cp. Section 4.3.2). A Summary of the fit results is given in Table 4.4.

	π^-	π^+
λ parameter	0.662(7)	0.96(5)
R_{out}	2.0801(19) fm	1.91(24) fm
R_{side}	1.4584(40) fm	1.30(6) fm
R_{long}	1.484(8) fm	1.79(15) fm

Table 4.4: The result of the three dimensional fit with Equation 3.14 for π^- and π^+ are summarized in this Table.
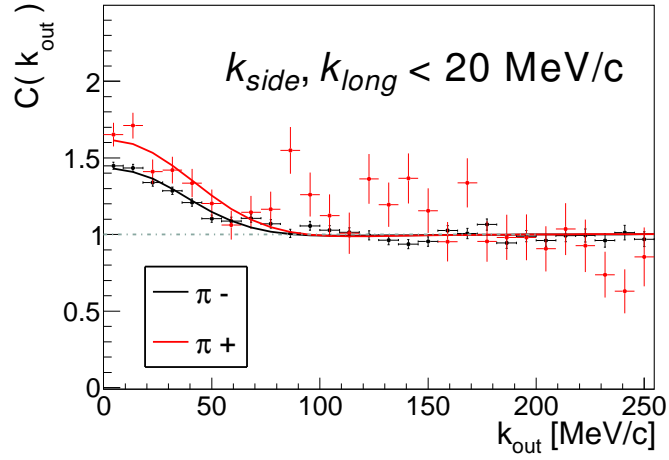
(a) Correlation strength between the identical pion pairs in out-direction.
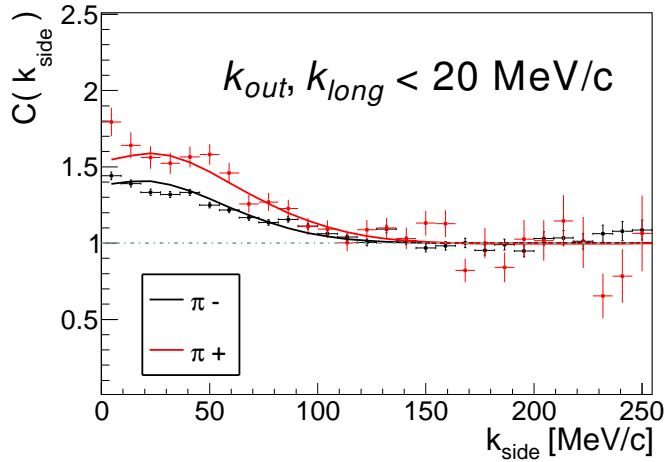
(b) Correlation strength between the identical pion pairs in side-direction.
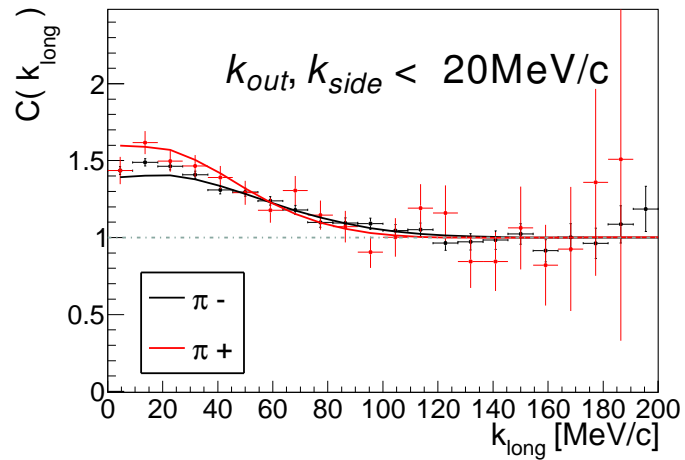
(c) Correlation strength between the identical pion pairs in long-direction.

Figure 4.17: The three correlation functions for π^- (black) and π^+ (red) are fitted with Equation 3.14 in a range of 0 - 150 MeV/c.

Chapter 5

Results and Discussion

In this chapter the results of the three dimensional analysis are summarized, since they are the main issue of this thesis.

Due to a three-dimensional correlation analysis in a longitudinally co-moving system, we are able to extract the parameter $R_{out}, R_{side}, R_{long}$ and λ for correlations between two negative and between two positive charged pions. The results are summarized in Table 4.4.

The λ Parameter

The λ parameter for the positive pions is clearly bigger than the one for the negative pions. This is in line with the result for the λs in the one dimensional fit ($\lambda_{\pi^-} = 0.31$, $\lambda_{\pi^+} = 0.71$). Referring to the theoretical meaning of the λ parameter (Section 3.4.1), λ accounts the percentage of pions, which are Bose-Einstein correlated. A variation from unity can be caused by misidentified particles [17]. This means that the smaller λ for the negative charged pions can arise from misidentified electrons and especially muons (cp. Section 4.2.3). Due to the conservation of the lepton number, we can only produce single muons through a weak decay of a pion. Although $c\tau$ (7.8045m [3]) of the pions lays outside of the detector, a certain amount of the pions will decay within the aperture. Since there are more π^- than π^+, this effect will lead to an enhancement of negative charged muons. However the percentage of muons per corresponding pions should be similar. The fact that all other processes only produce $\mu^+\mu^-$ - pairs leads to the same number of additional muons for both charges. Since we have less π^+ this leads to a higher ratio of muons per pion for the positive charged particles. Thus, the higher purity of the positive pions must originate from the differences in PID cuts.

Furthermore we use the Bowler-Sinyukov parametrization, which assumes a Gaussian source. Especially for small sources this has not to be the case and since that it is also possible that the λ parameter is smaller than unity because the source isn't Gaussian.

The Radii

Since the source of the pions isn't static, the fitted radii cannot simply be equalized to the space dimensions. They describe the space and time depended region where the emitted pions interact until they freeze out and fly into the detector. This region can be parametrized by the four vector $x_\mu = (x, y, z, t)$, which gives the space time coordinates of the last interaction of the pion pair relative to the effective source center. The transverse velocity of the pion pair is given by β_t and the longitudinal velocity by β_l. With this quantities one can calculate the radii like the following [21].

$$R_{side}^2 = \left\langle y^2 \right\rangle, \tag{5.1a}$$

$$R_{out}^2 = \left\langle (x - \beta_t t)^2 \right\rangle, \tag{5.1b}$$

$$R_{long}^2 = \left\langle (z - \beta_z t)^2 \right\rangle, \tag{5.1c}$$

R_{side} correlates most directly with the source geometry, because we have no motion of the pion pair into this direction. Therefore one can conclude that the source of pions has a geometrical radius of R_{side} into the direction orthogonal to the beam and orthogonal to the transverse velocity of the pion pair. This means a size of 1.46 fm for $\pi^-\pi^-$ and 1.30 fm for $\pi^+\pi^+$. These values are in accordance to the order of magnitude of the radii determined by the one dimensional analysis, which are 1.40 fm for $\pi^-\pi^-$ and 1.22 fm for $\pi^+\pi^+$. Furthermore, values of a few fm represent a realistic source volume compared to the size of the system consisting of a tungsten nucleus ($^{183.8}_{74}$W) with a radius of about $1.3 \cdot A^{1/3} = 5.46$ fm and a pion with a charge radius of about 0.67 fm [3]. In heavy ion collision radii of 2 - 6 fm are measured [15], since the system is much bigger. Altogether the measured values for R_{side} are in the right order of magnitude.

The other both radii R_{long} and R_{out} are dependent of the velocity of the particle pair and the duration t of the emission. Because of that we are not able to make any conclusions for the geometrical volume yet. One could use simulated data with known reaction locations to solve this problem. If one finds a connection between radii and the absorption location for simulated data, it might be possible to draw conclusions from these results to the geometric source of the measured pions.

The differences of the radii of the π^- and π^+ sources can either be caused by a really different size of the correlation regions or systematic errors. It is likely that the values will lay within each others errors after adding systematic uncertainties, because we expect the same behavior for both particle types.

Chapter 6

Conclusion and Outlook

Altogether one can say that it's possible to extract information about the source of produced pions from the $\pi^- + W$ data of the HADES experiment. We were able to extract spatio-temporal radii of the pion emitting source by performing a three dimensional correlation analysis. However we cannot make clear statements about the form of absorption location of the produced pions, since we are not able to determine the geometric dimensions of the pion emitting source due to its time dependence. In the future it might be possible to solve this problem with the help of simulations.

To improve the results in general the finite momentum resolution of the detector has to be taken into account. Furthermore systematic errors have to be added. At the end of the analysis the result has to be stable. In Figure 4.11 the correlation functions for higher relative momenta are shown. The strange behavior especially for negative pions should be resolved in the future, too. Afterwards the same analysis can be applied to $\pi^- + C$ data, which was taken in the same run of HADES. Since the Carbon nucleus is smaller, one expects a smaller absorption region which could lead to smaller radii.

Appendix A

Appendix

An illustration that the fitting procedure for the graphical energy loss versus momentum cut stays constant, is given in the following Figures.
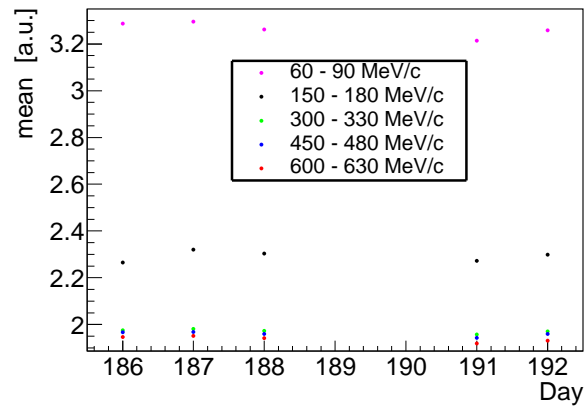
Figure A.1: The means of some fitted example slices for the π^- cut are plotted for data from the different days. Day 189 and 190 are left out because they include to few statistics for this fitting procedure, but for the other days the value stays constant.
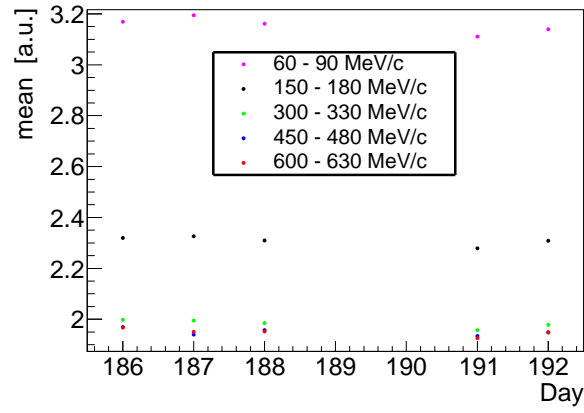
Figure A.2: The means of some fitted example slices for the π^+ cut are plotted for data from the different days. Day 189 and 190 are left out because they include to few statistics for this fitting procedure, but for the other days the value stays constant.
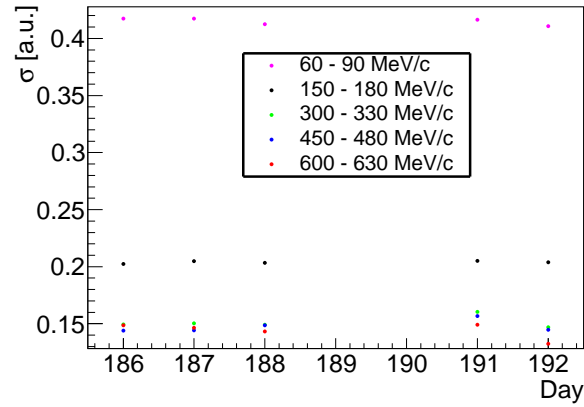
Figure A.3: The σs of some fitted example slices for the π^- cut are plotted for data from the different days. Day 189 and 190 are left out because they include to few statistics for this fitting procedure, but for the other days the value stays constant.
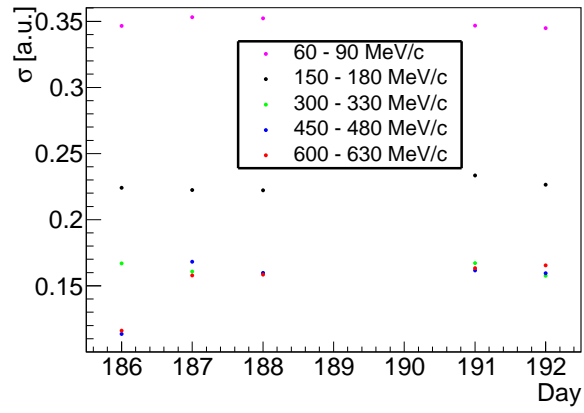
Figure A.4: The σs of some fitted example slices for the π^+ cut are plotted for data from the different days. Day 189 and 190 are left out because they include to few statistics for this fitting procedure, but for the other days the value stays constant.
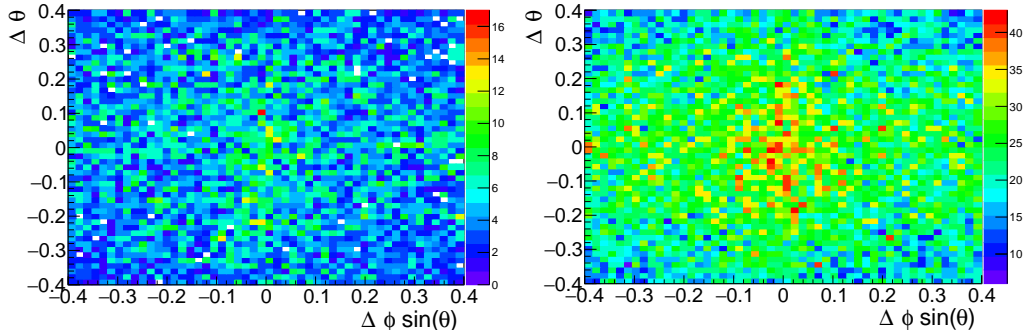
(a) angular distribution for positive pion pairs from the same event.

(b) angular distribution for positive pion pairs from mixed events.
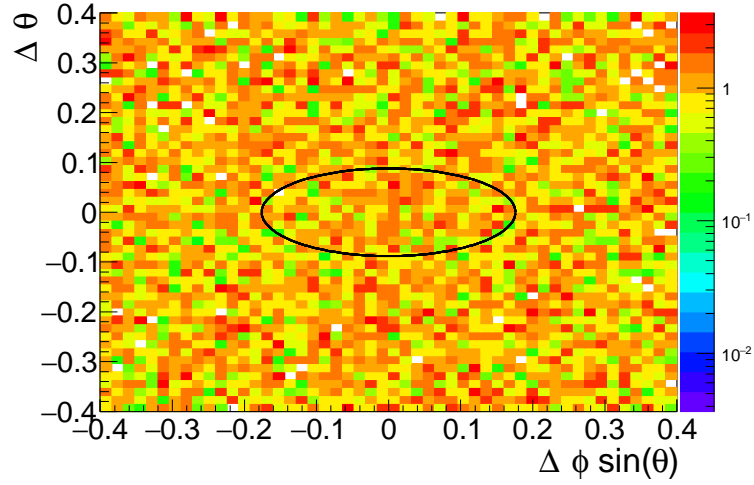
(c) The logarithmic ratio of distribution (a) and distribution (b) makes the lack clearly visible.

Figure A.5: The relative, angular distributions are shown for positive pion pairs from the same event (a) and mixed events (b). The lower plot shows the ratio of both. The suppressing of too close pairs through track merging is not visible due to the worse statistic.
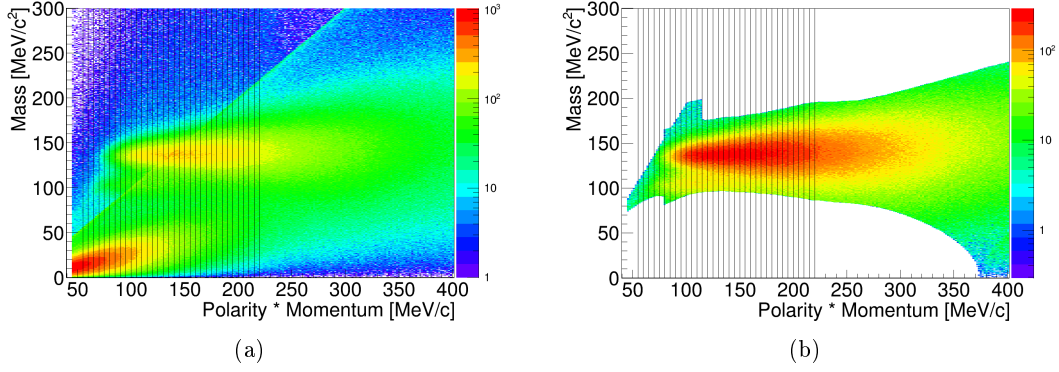
Figure A.6: The mass versus momentum distribution after the two steps (MDC cut, MDC + TOF cut) of the particle identification are plotted for positive pions. They are divided into momentum slices of 5 MeV/c by the black lines.
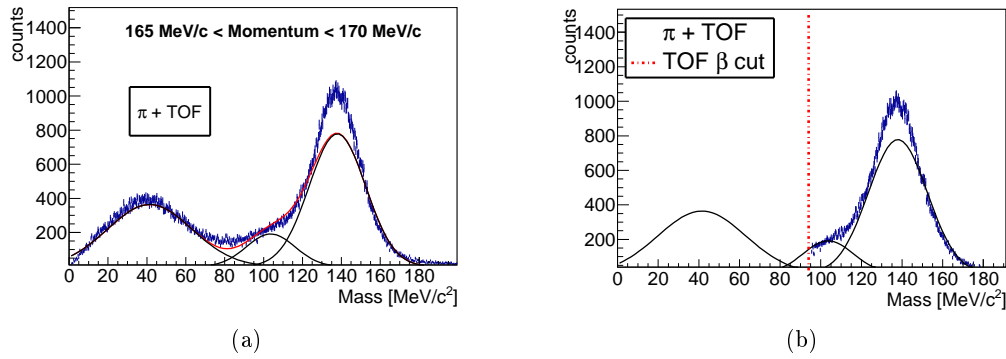
Figure A.7: One example slice for the TOF data is shown for positive pions. The fit does not describe the pion peak perfectly. Since it is smaller, the purity is underestimated For the TOF data.

(a)

(b)

(c)

(d)
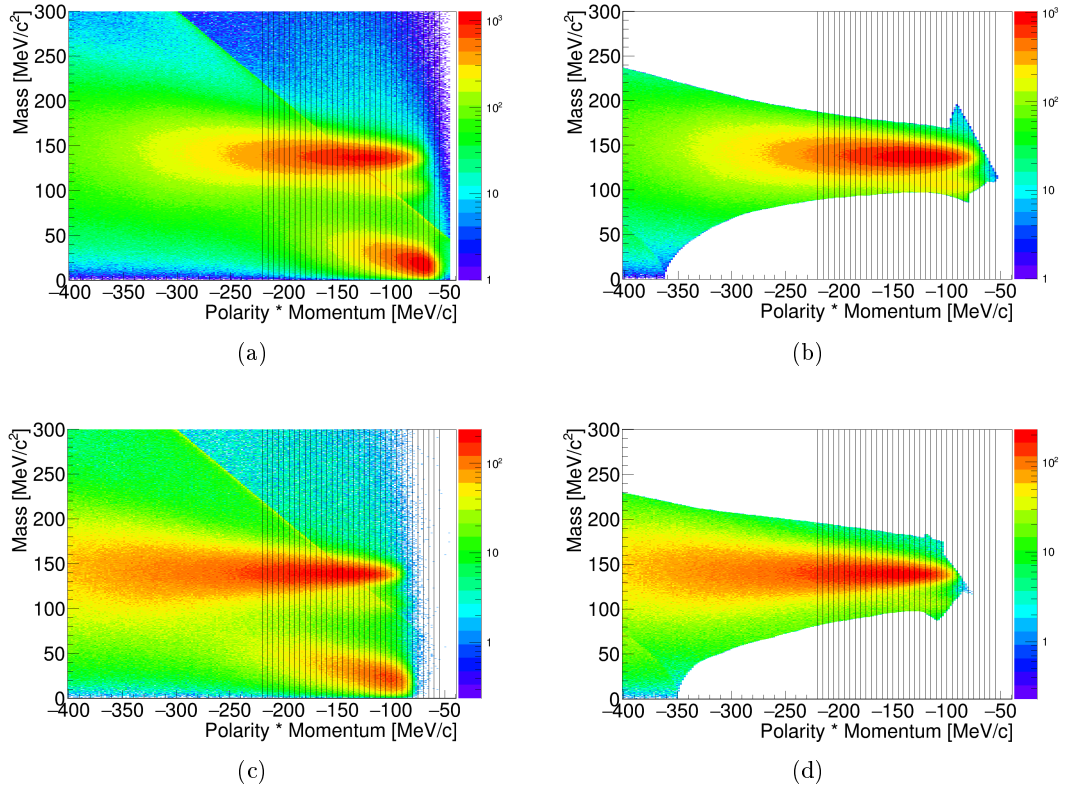
Figure A.8: The mass versus momentum distribution after the two steps (MDC cut, MDC + TOF/RPC cut) of the particle identification are plotted for negative pions. They are divided into momentum slices of 5 MeV/c by the black lines and fitted in the same way as the positive pions.

Bibliography

[1] G. Occhialini and C. Powell. Nuclear disintegrations produced by slow charged particles of small mass. *Nature*, 159(186-190):3, 1947.

[2] D.H. Perkins. Nuclear disintegration by meson capture. *Nature*, 159(4030):126–127, 1947.

[3] K. A. Olive et al. Review of Particle Physics. *Chin. Phys.*, C38:090001, 2014. `doi:10.1088/1674-1137/38/9/090001`.

[4] Laura Fabbietti. Pion induced reactions: strangeness programme. 2014. Presented at the workshop "Achievements and perspectives in the low-energy QCD with strangeness".

[5] M. L. Benabderrahmane et al. Measurement of the in-medium K^0 inclusive cross section in π^--induced reactions at 1.15 GeV/c. *Phys. Rev. Lett.*, 102:182501, May 2009. URL: `http://link.aps.org/doi/10.1103/PhysRevLett.102.182501`, `doi:10.1103/PhysRevLett.102.182501`.

[6] G Agakichiev et al. The high-acceptance dielectron spectrometer hades. *The European Physical Journal A*, 41(2):243–277, 2009.

[7] GSI. Hades website, August 2015. URL: `https://www-hades.gsi.de/`.

[8] J Michel et al. The upgraded hades trigger and data acquisition system. *Journal of Instrumentation*, 6(12):C12056, 2011. URL: `http://stacks.iop.org/1748-0221/6/i=12/a=C12056`.

[9] J. Dıaz et al. Design and commissioning of the gsi pion beam. *Nuclear Instruments and Methods in Physics Research Section A: Accelerators, Spectrometers, Detectors and Associated Equipment*, 478(3):511–526, 2002.

[10] Kclus website, August 2015. URL: `https://www.e12.ph.tum.de/groups/kcluster/ResearchTopic5.php`.

[11] R. Hanbury-Brown, R. Q. Twiss, et al. A test of a new type of stellar interferometer on sirius. *Nature 178, 1046*, 1956.

[12] M. A. Lisa. *Impact Parameter-Gated Two-Proton Intensity Interferometry in Intermediate Energy Heavy Ion Collisions.* PhD thesis, MICHIGAN STATE UNIVERSITY., 1993.

[13] G. Baym et al. The Physics of Hanbury Brown-Twiss intensity interferometry: From stars to nuclear collisions. *Acta Phys. Polon.*, B29:1839–1884, 1998. `arXiv:nucl-th/9804026`.

[14] G. Goldhaber et al. Influence of bose-einstein statistics on the antiproton-proton annihilation process. *Phys. Rev. 120, 300*, 1960.

[15] M. A. Lisa et al. Femtoscopy in relativistic heavy ion collisions: Two decades of progress. *Annual Review of Nuclear and Particle Science*, 55(1):357–402, 2005. URL: `http://dx.doi.org/10.1146/annurev.nucl.55.090704.1515 33`, `doi:10.1146/annurev.nucl.55.090704.151533`.

[16] M.G. Bowler et al. Extended sources, final state interactions and bose-einstein correlations. *Zeitschrift für Physik C Particles and Fields*, 39(1):81–88, 1988. URL: `http://dx.doi.org/10.1007/BF01560395`, `doi:10.1007/BF01560 395`.

[17] J. Adams et al. Pion interferometry in au+au collisions at $\sqrt{s_{NN}} = 200$ GeV. *Phys. Rev. C*, 71:044906, Apr 2005. URL: `http://link.aps.org/doi/10.11 03/PhysRevC.71.044906`, `doi:10.1103/PhysRevC.71.044906`.

[18] HADES Collaboration. Hydra class documentation, September 2015. URL: `http://web-docs.gsi.de/~halo/docs/hydra/classDocumentation/dev/ind ex.html`.

[19] H. Bethe. Theory of the passage of fast corpuscular rays through matter. *Annalen Phys.*, 5:325–400, 1930.

[20] S.A. Bass et al. Microscopic models for ultrarelativistic heavy ion collisions. *Progress in Particle and Nuclear Physics*, 41:255 – 369, 1998. URL: `http://www.sciencedirect.com/science/article/pii/S0146641098000581`, `doi:http://dx.doi.org/10.1016/S0146-6410(98)00058-1`.

[21] Y.-F. Wu, U. Heinz, B. Tomášik, and Wiedemann. Yano-koonin-podgoretskii parametrisation of the hanbury brown-twiss correlator. *The European Physical Journal C - Particles and Fields*, 1(3):599–617, 1998. URL: `http://dx.doi. org/10.1007/s100520050109`, `doi:10.1007/s100520050109`.

Acknowledgment